

CHARGED-PARTICLE TRANSPORT IN
TURBULENT MAGNETIC FIELDS

by
Peng Sun

Copyright © Peng Sun 2016

A Dissertation Submitted to the Faculty of the

DEPARTMENT OF PLANETARY SCIENCES

in Partial fulfillment of the Requirements
For the Degree of

DOCTOR OF PHILOSOPHY

in the Graduate College

THE UNIVERSITY OF ARIZONA

2016

THE UNIVERSITY OF ARIZONA
GRADUATE COLLEGE

As members of the Dissertation Committee, we certify that we have read the dissertation prepared by Peng Sun, titled Charged-Particle Transport in Turbulent Magnetic fields and recommend that it be accepted as fulfilling the dissertation requirement for the Degree of Doctor of Philosophy.

Jack Randy Jokipii Date: _____
Apr 25, 2016

Renu Malhotra Date: _____
Apr 25, 2016

Joe Giacalone Date: _____
Apr 25, 2016

Roger Yelle Date: _____
Apr 25, 2016

Adam Showman Date: _____
Apr 25, 2016

Final approval and acceptance of this dissertation is contingent upon the candidate's submission of the final copies of the dissertation to the Graduate College.

I hereby certify that I have read this dissertation prepared under my direction and recommend that it be accepted as fulfilling the dissertation requirement.

Dissertation Director: Jack Randy Jokipii Date: _____
Apr 25, 2016

STATEMENT BY AUTHOR

This dissertation has been submitted in partial fulfillment of the requirements for an advanced degree at the University of Arizona and is deposited in the University Library to be made available to borrowers under rules of the Library.

Brief quotations from this dissertation are allowable without special permission, provided that an accurate acknowledgement of the source is made. Requests for permission for extended quotation from or reproduction of this manuscript in whole or in part may be granted by the copyright holder.

SIGNED: PENG SUN

ACKNOWLEDGEMENT

I would like to gratefully acknowledge the unlimited support and guidance of the faculty members and my committee members at the University of Arizona, and especially my advisor Dr. Jack R Jokipii. His deep insight and keen senses of physics encouraged and guarded me to finally find a feasible and safe path through the journey of my exploration. Without his supervision and guidance, I would never have had the confidence and determination to solve such a complicated problem in my PHD.

I am also grateful to Dr. Joe Giacalone, Dr. Jozsef Kota, and Dr. Federico Fraschetti for the helpful discussions that enriched the research of this dissertation. I would also like to give my thanks to Mary Guerrieri, Pam Street, John Pursch, Erica McEvoy, Xianyu Tan, etc. from the Department of Planetary Science for their help throughout my PHD.

Finally, my deepest thanks go to my wonderful wife Eva, my lovely daughter Emily and my adorable son Eddie. With my fantastic family, I never felt alone during this journey but full of joy and gratefulness.

Contents

List of Figures	8
List of Tables	10
Abstract	11
Chapter 1 Introduction	14
1.1 Origins of the problem	15
1.2 The current understanding	18
1.3 New challenges	23
1.4 Outline of the dissertation	25
Chapter 2 Solar Wind Turbulence	27
2.1 Introduction	28
2.2 Magnetic Field Model	29
2.3 Tracking the Energetic charged particles	34
2.4 Determining the pitch-angle diffusion coefficient	35
2.5 Results	37

2.6	Conclusion	43
Chapter 3	Global Anisotropy	44
3.1	Synthesis of the magnetic fields	46
3.2	Numerical method and parameters	47
3.3	Results	51
3.4	Conclusion	55
Chapter 4	Local Anisotropy	57
4.1	Introduction	58
4.2	A Multi-Scale Synthesis of the Magnetic Field	60
4.3	Synthesis of the Two Scale Anisotropy	68
4.4	Transport Experiments and Results	72
4.5	Conclusion	75
Chapter 5	Applications to Solar Wind data	76
5.1	Introduction	77
5.2	Data process techniques and assumptions	79
5.3	Power Spectrum Synthesis	81
5.4	Results	83
5.5	Conclusion	84
Chapter 6	Summary	85
Appendix A	Numerical Integrators	89

Bibliography 94

List of Figures

1.1	Cosmic Rays flux	16
1.2	ACRs in the heliosphere	17
1.3	Charged particle motion in a uniform magnetic field.	19
2.1	A sliding window experiment	34
2.2	$\mathbf{D}_{\mu\mu}$ vs charged particle energy	38
2.3	$\mathbf{D}_{\mu\mu}$ vs the magnetic field turbulence strength	40
3.1	Power spectra of the GS model	45
3.2	Transport coefficients vs E_p in the Global Anisotropy	50
3.3	Transport coefficients vs σ_B^2 in the Global Anisotropy	52
4.1	A schematic plot showing the division of wavenumber	60
4.2	An example of local synthesis	65
4.3	Transport coefficients in the field with local anisotropy	72
5.1	Schematic plot of the power spectrum extraction algorithm from a time series data set	78

5.2	The synthesized power spectra for the large and small scales . . .	81
A.1	Algorithm Test1: Two Body problem	91
A.2	Algorithm Test2: Restricted Three Body problem	93

List of Tables

2.1	Parameters for scattering simulations	31
3.1	Global anisotropy transport numerical experiment parameters . .	49
4.1	Simulation parameters with the field synthesis of the local anisotropy	69

Abstract

Collisionless turbulence is common in astrophysical magnetic fields and plasmas. The determination of the transport of high-energy charged particles both parallel and perpendicular to the average magnetic field in such a system is of considerable interest. It is recognized that the turbulent magnetic field has important effects on the transport of charged particles and that the properties of different turbulence models may significantly affect the resulting transport properties. A number of different magnetic turbulence models have been proposed in the last several decades. We present here the results of a study of charged particle transport in two new turbulent magnetic field models that have not been previously considered and include newly described characteristics. We investigate the effect of energetic charged particle motion in these new models.

We use a method (D A Roberts, 2012) that optimizes phase angles of a set of circularly polarized, transverse modes with Kolmogorov power-law enveloped amplitudes to construct magnetic field fluctuations with nearly constant $|B|$ but with large variances in the components B_x , B_y , B_z , as is

observed in the Solar Wind. Charged particle scattering coefficients are determined through computer simulations. The results are compared with those from previous isotropic and composite turbulence models.

We studied charged particle transport in the turbulent magnetic field with global anisotropy and compared with the isotropic turbulence. We found that the magnetic turbulence with global anisotropy and isotropy have similar effects on charged particle transport from $1MeV$ up to $10GeV$.

We proposed a general framework for a multi-scale synthesis with the scale-dependent, localized anisotropic feature incorporated. We run test particle simulations in the field by the two-scale algorithm to calculate the transport coefficients for charged particles with different energies. We found that the local anisotropy has the significant difference from the previous model in the effect on charged particle transport. The parallel transport (κ_{\parallel}) decreases while the perpendicular transport (κ_{\perp}) increases compared with the isotropic and globally anisotropic field models, the difference is enhanced as the local anisotropy is enhanced, and there is an order of magnitude increase in the ratio of perpendicular to parallel transport coefficients.

We proposed a simple power spectrum synthesis method based on the Fourier analysis to extract the large and small scale power spectrum from any single spacecraft observation with a long enough period and a high sampling frequency. We applied the method to the solar wind measurement by the magnetometer onboard the ACE spacecraft and reconstructed the large scale

isotropic 2D spectrum and the small scale anisotropic 2D spectrum.

Chapter 1

Introduction

The dissertation covers two related major topics: 1) the investigation of the charged particle scattering in a solar wind like turbulent magnetic field, and 2) the synthesis framework of anisotropic magnetic turbulence and the calculation of the charged particle. The connections which link these topics together lie in the answers to the following questions: how do charged particles transport in different kinds of magnetic turbulence? What are the differences and similarities? Given different turbulence models, how do we realize each field model practically? How to design numerical experiments to calculate the transport? What are the underlying physics for charged particle transport in different turbulence models? In this chapter, I will review the current research status on charged particle transport and then point out the unsolved problems and possible directions.

1.1 Origins of the problem

Our understanding of the universe is mainly based on the observations of the electromagnetic emission from various astronomical sources, most of which are in the plasma state with high temperature and degree of ionization. Radiation processes associated with energetic particles include the interactions with other particles, magnetic fields, and photons, etc. One of the key aspects to understand these processes is the spatial and energy distribution of the energetic charged particles in the sources. Therefore, it is of great interest to understand how and where charged particles are energized by various sources and transported through different mediums. In this dissertation, we mainly focus on the energetic charged particle transport and the related phenomena.

Energetic charged particles can be divided into different classes by their origins, such as the Solar Energetic Particles (SEPs) coming from the Sun, Galactic Cosmic Rays (GCRs) from the galaxy, and Anomalous Cosmic Rays (ACRs) from the boundary of the heliosphere. Figure 1.1 shows the energy spectrum of the Cosmic Rays flux observed at the ground level on earth (Beatty & Westerhoff, 2009). The GCRs with high enough energy as 10^{20} eV, when hitting the atmosphere, would cause the air shower of secondary particles and photons. However, before early 20th century, people believed that the source of the nuclear radiations in the atmosphere are from the earth and would decrease with the altitude. The Nobel Laureate Victor Hess, during his in person adventurous balloon flight in 1911-1912, systematically measured the

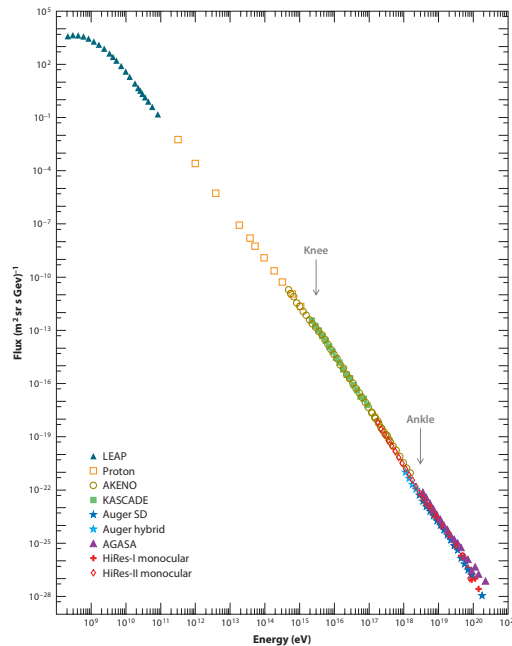


Figure 1.1: The general Cosmic Rays flux energy spectrum from ground level observations summarized in Beatty & Westerhoff (2009). Notice the steepening 'knee' at about $10^{15}eV$ and the flattening 'ankle' at about $10^{18}eV$. The knee is thought to be related to the limited acceleration ability at certain supernovae, and the ankle is hypothesized to be of extra-galactic origin.

radiation levels in the atmosphere up to 5.3 km above the ground. Based on his measurements he proposed that "The results of these observations seem best explained by a radiation of great penetrating power entering our atmosphere from above" (Hess, 1912). This discovery opened the research of high energy cosmic charged particles.

The research on charged particle transport reveals the underlying dynamics of astrophysical phenomena. GCRs are modulated by the solar wind, and the modulation correlates with the 11-year cycle of the solar wind flux. The

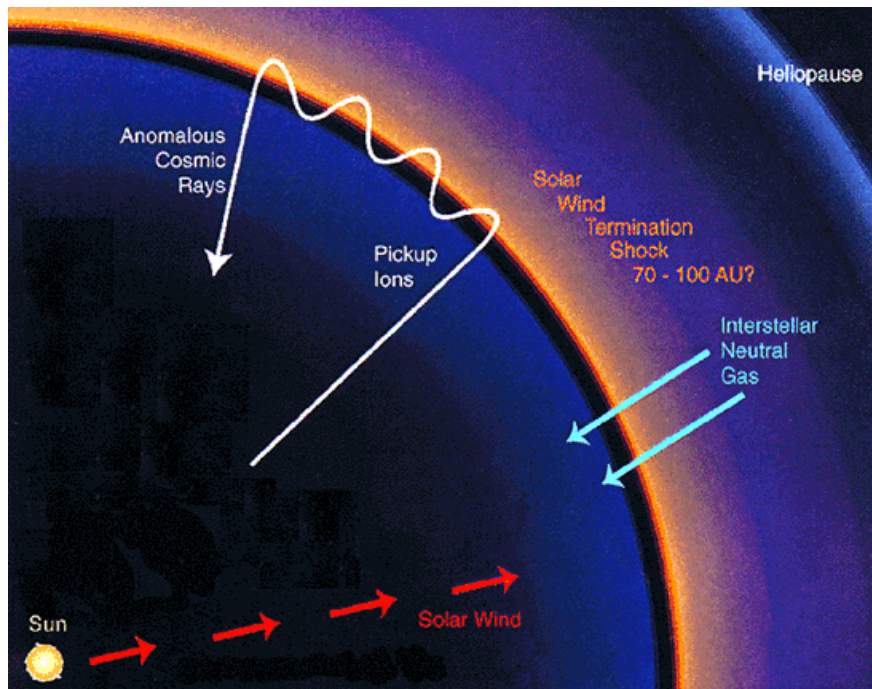


Figure 1.2: The schematic plot of the anomalous cosmic rays (ACRs). The red arrows shows that the charged particles in the solar wind are the radially flowing outward from the sun. The light blue arrows shows that the inward flowing interstellar neutral gas particles (e.g. hydrogen atoms) are not affected by the solar wind magnetic field. The white arrowed curve shows how a pickup ion, one of the two products of the charge exchange reaction between a solar wind ion and an interstellar hydrogen atom, will be picked up by the solar wind plasma flow and get accelerated near the solar wind termination shock at about 100 AU. Credit: NASA

ACRs, shown in Figure 1.2, are originally the cold interstellar neutral particles as they pass through the solar wind towards the inner heliosphere they are turned into ions by charge exchange reactions and get picked up by the solar wind. They are then accelerated at the boundary of the solar wind around 100AU and get a chance to propagate back to the earth. In this way, the ACRs act as a sample of the local interstellar medium near the solar system. ACRs also respond to the long term variation of the solar wind and GCRs. The SEPs are closely related to the solar flares or coronal mass ejections, those violent explosions in the solar atmosphere.

1.2 The current understanding

In a uniform magnetic field, charged particles will go through a cyclic helical motion parallel or anti-parallel to the magnetic field as in Figure 1.3. If the magnetic field has gradient and curvature, the guiding centre of the charged particle (the position averaged over the gyro periods) will have gradient and curvature drift motions. However, generally in the real astrophysical environment the magnetic field is so irregular down to the scale of the ion gyro-radius that the sole combination of helical and drifting motions may not be sufficient to completely describe the charged particle motions. A more suitable physical model would be to regard the individual motion of a charged particle as a random walk in the irregular magnetic field. This modern picture is developed from the charged particle acceleration theory, the Fermi

mechanism (Fermi, 1949), where interactions with the irregularities in the magnetic field are equivalently described as a series of scatterings created by the moving magnetic clouds. This Diffusion Approximation originated from the kinetic theory of ordinary gases. In the astrophysical environment, the Fermi acceleration mechanism is applied to account for the parallel shock accelerations on charged particles, where charged particles will be reflected and gain energy on either side of the shock to have the chance to cross the shock so many times that it can reach high energy before leaving the shock. The detail of the shock acceleration is beyond the scope of this dissertation. However, the Fermi mechanism, introducing the concept of a scattering time, suggests that particle's motion is the random walk and hence a statistical approach is adequate to describe it.

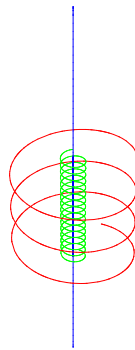


Figure 1.3: The charged particle motion in a uniform magnetic field. The blue line represents the magnetic field, the red line shows the trajectory of an ion and the green line shows the trajectory of an electron.

The general equation that describes the particle going through a series

of random scatterings is the Fokker-Planck equation, where the motion of a particle is represented by the evolution of the probability density function representing the particle distribution over the phase space of interest.

$$\frac{\partial f}{\partial t} = - \sum_i^n \frac{\partial}{\partial X_i} \left[\frac{\langle \Delta X_i \rangle}{\Delta t} f \right] + \sum_i^n \frac{\partial^2}{\partial X_i^2} \left[\frac{\langle \Delta X_i^2 \rangle}{2\Delta t} f \right] \quad (1.1)$$

Here f is the probability density function and X_i is the i_{th} dimension of an n -dimensional phase space. For example, if $(X_1, X_2, X_3, X_4, X_5, X_6) = (x, y, z, u, v, w)$ were to specify the phase space of a particle's position and velocity, the equation (1.1) would describe the behavior of an ensemble of such particles experiencing the drift and diffusion in the position/velocity phase space. In the context of the solar wind, where a plasma flow carries the magnetic field blowing out of the sun, the governing equation for the transport of the energetic charged particles is the Parker's transport equation

$$\frac{\partial f}{\partial t} = \nabla \cdot (\kappa_{ij}^S \cdot \nabla f) - (v_d + U) \cdot \nabla f + \frac{p}{3} (\nabla \cdot U) \frac{\partial f}{\partial p} \quad (1.2)$$

Here κ_{ij}^S is the symmetric part of the diffusion tensor for the energetic charged particles, v_d is their drifting velocity, p their momentum, and U the solar wind velocity. Notice that the isotropy of the energetic charged particles in their momentum space is assumed. Given the transport coefficients determined by the observables, such as the parameters of the plasma flows and the magnetic fields, one is able to calculate the evolution of the energetic charged particles correspondingly. So now the problem is how to quantitatively determine the transport coefficients $(\frac{\langle \Delta X_i^2 \rangle}{2\Delta t})$ as defined in the Fokker-Planck equation and

κ_{ij}^S as in the Parker's transport equation), which are intricately related to the quantitative description of the irregular magnetic fields.

The magnetic field in the astrophysics environment is often approximated by a mean plus a random part

$$\mathbf{B} = \mathbf{B}_0 + \delta\mathbf{b} \quad (1.3)$$

Statistically, the full description of the random field requires the information from all the multi-point correlation functions such as $\langle \mathbf{B}(\mathbf{X}) \rangle$, $\langle \mathbf{B}(\mathbf{X}_i)\mathbf{B}(\mathbf{X}_j) \rangle$, $\langle \mathbf{B}(\mathbf{X}_i)\mathbf{B}(\mathbf{X}_j)\mathbf{B}(\mathbf{X}_k) \rangle$, ..., etc. Physically, it depends on the understanding of the different magnetic turbulence models. For quite a long time, people believe that the turbulence in the astrophysical environment is of the Kolmogorov type. It is isotropic, and the power spectrum follows the Kolmogorov's $-5/3$ law (Kolmogorov, 1941). Observations suggest that the $5/3$ power law applies across several orders of magnitude in the spatial scales (Armstrong et al., 1995).

Jokipii (1966) first investigated the transport in this kind of turbulent magnetic field by utilizing a quasilinear approach such that, when a particle moves in the weak turbulent magnetic field, its motion could be decomposed into a gyration around the mean field plus a random walk along the field lines. He showed explicitly how the coefficients are related to the power spectra of the turbulent magnetic field, given that the magnetic turbulence is axisymmetric and its two-point correlation function is of the greatest interest. Physically the power spectrum of the turbulent magnetic field follows the

Kolmogorov's 5/3 law, or in another word, the magnetic turbulence is of Kolmogorov type. This quasilinear theory provides a clear and appealing physical picture of the energetic charged particle transport in a weak turbulent magnetic field. In this case the transport coefficients are

$$\kappa_{\parallel} = \frac{2w^2}{9} \left[\int_0^1 \frac{\langle \Delta \mu^2 \rangle}{\Delta t} d\mu \right]^{-1} \quad (1.4)$$

$$\frac{\langle \Delta \mu^2 \rangle}{\Delta t} = \frac{1 - \mu^2}{|\mu|w} \frac{Z^2 e^2}{\gamma^2 m^2 c^2} P_{xx} \left(k = \frac{\omega_0}{\mu w} \right) \quad (1.5)$$

$$\kappa_{\perp} = \frac{1}{2} \int_0^1 \frac{\langle \Delta x^2 \rangle}{\Delta t} d\mu \quad (1.6)$$

$$\frac{\langle \Delta x^2 \rangle}{\Delta t} = \frac{\langle \Delta y^2 \rangle}{\Delta t} = \left[\frac{\mu w}{B_0^2} P_{xx}(k=0) + \frac{(1 - \mu^2)w}{2|\mu|B_0^2} P_{zz} \left(k = \frac{\omega_0}{\mu w} \right) \right] \quad (1.7)$$

Here w is particle's speed, μ its cosine of pitch angle (the angle between its velocity and the local magnetic field), Z the charge number, e the charge unit, γ the Lorentz factor, m its mass, c the light speed, ω its gyro frequency in the mean field, P the power spectrum function along x or z direction, k the wave number, and B_0 the mean magnetic field in the z direction in this case. Using the parallel and perpendicular transport coefficients κ_{\parallel} and κ_{\perp} , and assuming that the pitch angle distribution is near isotropy and the drifting motions are neglected, the above Fokker-Planck equation could be rewritten as

$$\frac{\partial f}{\partial t} = \kappa_{\parallel} \frac{\partial^2 f}{\partial z^2} + \kappa_{\perp} \left[\frac{\partial^2 f}{\partial x^2} + \frac{\partial^2 f}{\partial y^2} \right] \quad (1.8)$$

However, the observations of the magnetic field in the solar wind suggests that the magnetic turbulence is non-isotropic (Dobrowolny et al., 1980; Shebalin et al., 1983). There are slab modes plus two dimensional modes in the turbulent magnetic field hence is called the composite turbulence, and

the ratio between the power of the slab modes and that of the 2D modes is found to be about 1 : 4 (Matthaeus et al., 1990; Tu & Marsch, 1993; Bieber et al., 1996). This turbulence model emphasizes the transverse complexity of the magnetic field, leading to the rapid separation of the field lines, which is especially important to the particle transport (Jokipii, 1973). Matthaeus et al. (2003) proposed the nonlinear guiding center theory to describe and calculate the charged particle's diffusion in the composite magnetic turbulence. The perpendicular transport coefficient is shown to be (Matthaeus et al., 2003)

$$\kappa_{xx} = \frac{a^2 v^2}{3B_0^2} \int \frac{S_{xx}(\mathbf{k}) dk_x dk_y dk_{\parallel}}{\frac{v}{\lambda_{\parallel}} + (k_x^2 + k_y^2) \kappa_{xx} + k_{\parallel}^2 \kappa_{zz}} \quad (1.9)$$

Here a is a parameter to be fitted, S_{xx} the static power spectrum function of the magnetic field, and λ_{\parallel} the parallel mean free path.

1.3 New challenges

Observations from the time series of the magnetometer data of the solar wind show that the variance of the solar wind magnetic field's magnitude ($|B|$) is usually much smaller than the magnitude of its components (e.g. B_x , B_y , B_z). Whether this could affect the scattering and diffusion of the charged particles is of great interest; however, it is difficult to describe this kind of magnetic field in a viable mathematical form, or even in computer simulations of the solar wind. The only possible way to generate this kind of turbulence is the synthesis method. The synthesis method is used to generate the isotropic, slab

and 2D turbulent magnetic field (Giacalone & Jokipii, 1999; Matthaeus et al., 2003). And it is not until 2012 that Roberts (2012) proposed a feasible method to generate this type of turbulent magnetic field with a small variance of the field magnitude. This makes possible the calculation of the charged particle transport in the magnetic field of the solar wind type.

Another challenge comes from the advancement of the MHD turbulence theory. In the Goldreich-Sridhar model (Goldreich & Sridhar, 1995), for incompressible turbulence, in the inertial range the turbulence cascade is also anisotropic. Consider a coherent structure within the inertial range of the MHD turbulence. In this structure (or simplified as eddy), the mixing of perpendicular and parallel modes (relative to the local mean magnetic field) are connected by the assumption that $k_{\parallel} V_A$ is in the same order as $k_{\perp} v_k$, where k_{\parallel} is the parallel wave number, V_A the Alfvén speed, k_{\perp} the perpendicular wave number, v_k the speed of the eddy at the scale of wave number k_{\perp} in the normal direction. This relation between k_{\parallel} and k_{\perp} in the local reference frame is based on the following arguments: 1) the parallel wave modes are traveling at Alfvén speed along the field line while the normal components at speed v_k , 2) the parallel cascading time scale is $(k_{\parallel} V_A)^{-1}$ while the perpendicular cascading time scale is $(k_{\perp} v_k)^{-1}$. The critical balance condition is that these two time scales are equal to each other. At this mixing rate the cascading energy is equal in both direction. This anisotropy changes the magnetic field and hence could change the scattering and diffusion of energetic particles

from the isotropic case. Another feature of interest is the scale dependence of the anisotropy. If we use the power spectra function to describe the anisotropy, the scale dependence means the power spectra function of the turbulence is not only a function of wave numbers as in the isotropic case, but also the mean magnetic field averaged at the scale associated with the corresponding wave numbers. This implies that the locally averaged field line, which differs from one scale/place to another, determines the shape and orientation of an eddy. This is quite different from the picture of the spatially homogeneous orientationally isotropic ordinary turbulence. How do the charged particles transport in this kind of turbulent magnetic field is of great interest and technical difficulty. A successful synthesis method which incorporates all the features would not only enhance our understanding of the organization and structure of the GS type turbulence, but also shed a light on the advancement and completeness of the existing charged particle transport theory.

1.4 Outline of the dissertation

Chapter 2 calculates charged particle's scattering in the solar wind type magnetic turbulence and compare the results with the isotropic turbulence. Chapter 3 describes the globally anisotropic turbulence. Chapter 4 presents the multi-scale synthesis of the locally anisotropic magnetic turbulence. Chapter 5 introduces a method to synthesize the 2D power spectra of the magnetic field from the time series observations of the magnetic field onboard a spacecraft.

Chapter 6 is the summary of the dissertation and the outline of the future work.

Chapter 2

Solar Wind Turbulence

We use a new method developed by Roberts (2012), that optimizes the phase angles of an ensemble of linearly polarized plane waves with amplitudes determined from a Kolmogorov-like power spectrum, to construct magnetic field vector fluctuations having nearly constant magnitude and large variances in its components. This representation of the turbulent magnetic field is consistent with that observed in the solar wind. Charged particle pitch-angle diffusion coefficients are determined by integrating the equations of motion for a large number of charged particles moving under the influence of forces from our pre-defined magnetic field. We tested different cases in which we varied the kinetic energy of the particles and the turbulent magnetic field variance. And for each combinations of test particle energies and turbulent magnetic field strengths, we tested three different models: 1) the so-called "slab" model in which the turbulent magnetic field depends on only one spatial coordinate and has significant fluctuations in its magnitude $(\delta B_x(z), \delta B_y(z), B_0)$, 2) the slab

model optimized with nearly constant magnitude ($b = \sqrt{\delta B_x^2 + \delta B_y^2 + B_0^2}$) and, 3) the slab model magnetic field with nearly constant magnitude plus a "variance-conserving" adjustment. In the case of the latter, this model attempts to conserve the variance of the turbulent components ($\sigma_{B_x}^2 + \sigma_{B_y}^2$), which is found to decrease during the optimization with nearly constant magnitude. We found that there is little or no effect on the pitch-angle diffusion coefficient $D_{\mu\mu}$ between the model 1) and 2). However, the result from model 3) is significantly different. We also introduce a new method to accurately determine the pitch-angle diffusion coefficients as a function of μ .

2.1 Introduction

As introduced in Chapter 1, the transport of high-energy charged particles in the Heliosphere, including galactic cosmic rays and solar-energetic particles is known to be affected significantly by the random or turbulent component of the interplanetary magnetic field embedded in the solar wind. The distribution of these particles in space, time and energy is governed by the cosmic-ray transport equation (Parker, 1965), which requires transport coefficients that depend on solar wind turbulence. The study of the turbulent interplanetary magnetic field is an active area of research (Dobrowolny et al., 1980; Matthaeus et al., 1990; Tu & Marsch, 1993; Dasso et al, 2005; Podesta et al, 2007; Horbury et al., 2008) and there are a number of different models that have been discussed (Tu & Marsch, 1993; Bieber et al., 1996; Boldyrev, 2006; Horbury et al.,

2008). It is important to understand how transport coefficients computed from the motion of particles depend on these different turbulence models. Besides theoretical completeness, this study is also applicable to the prediction of energetic particle intensities during increased solar wind activity, and is also relevant to the propagation of cosmic rays in the galactic magnetic field.

Observations show that the variance of the magnitude of the magnetic field in solar-wind turbulence is much smaller than the variance of its components (Belcher & Davis, 1971; Roberts, 2012). This feature of the solar wind turbulence has not been previously considered when deriving transport coefficients of charged particle transport in magnetic turbulence (Jokipii, 1966; Matthaeus et al., 2003). Previous numerical calculations (Giocalone & Jokipii, 1999) have considered a number of turbulence models including isotropic, composite (Matthaeus et al., 1990; Tu & Marsch, 1993; Bieber et al., 1996), and anisotropic (Goldreich & Sridhar, 1995) magnetic turbulence, but none of these models minimize the variance of the magnitude of the magnetic field. In this study, we adopt a new method, proposed by Roberts (2012), to synthesize magnetic turbulence with nearly constant magnitude and calculate diffusion coefficients of charged particles in this field.

2.2 Magnetic Field Model

We consider a magnetic field of the form $\mathbf{B} = \mathbf{B}_0 + \delta\mathbf{B}$, where \mathbf{B}_0 is the mean field and $\delta\mathbf{B}$ is a zero-mean random field. Since the energetic charged particle

is moving at a speed much higher than the Alfvén speed of disturbances along the magnetic field, it suffices to perform the transport simulations in multiple realizations of the static magnetic field. In order to produce a static field with nearly constant fluctuation in magnitude we follow the procedure described by Roberts (2012). For simplicity, but without loss of generality, we assume in the Cartesian coordinate system that the mean field is constant along z direction and that the random part of the turbulent magnetic field, $\delta\mathbf{B}$, is given by

$$\delta B_x(z) = \sum_n A(k_n) \sin(ik_n z + i\beta_n) \quad (2.1)$$

$$\delta B_y(z) = \sum_n A(k_n) \cos(ik_n z + i\theta_n) \quad (2.2)$$

where $A(k_n)$ represents the amplitude of the fluctuation and, k_n the wavenumber along the z axis, β_n and θ_n are the random phase angles of these two linear modes. The magnitude of the magnetic field, as a function of z , is given by

$$b(z) = \sqrt{\delta B_x^2(z) + \delta B_y^2(z) + B_0^2} \quad (2.3)$$

Note that $B_0 = \|\mathbf{B}_0\|$. We also note that $b(z)$ only depends on z , the direction of the average magnetic field. Because this is a one dimensional turbulent magnetic field, there are two ignorable coordinates, and it follows that charged particles must remain within one gyro-radius of the magnetic line of force in which it starts its motion (Jokipii et al., 1993). In this chapter we are concerned only with pitch angle diffusion.

The amplitudes in the sums given in equation (2.1) and (2.2) are deter-

mined from a one dimensional Kolmogorov spectrum given by

$$A^2(k_n) = CP(k_n)k_n \quad (2.4)$$

$$P(k_n) = \frac{1}{1 + (k_n L_c)^{5/3}} \quad (2.5)$$

where C is a normalization constant and, L_C is the correlation length of the magnetic fluctuations. The normalization is such that the total variance is $\delta\mathbf{B}$.

Simulation Parameters										
case	Energy	σ_B^2/B_0^2	N_m	N_c	N_p	R_w	N_b	Δt	Optimize	Scale Up
-	GeV	1	1	20000	1	1	2000	Ω^{-1}	flag	flag
1	10	.3	200	1	400	.05	1	.001	Off	Off
2	1	1	200	1	400	.05	1	.001	Off	Off
3	1	.3	200	1	400	.05	1	.001	Off	Off
4	1	.1	200	1	400	.05	1	.001	Off	Off
5	.1	.3	200	1	400	.05	1	.001	Off	Off
6	10	.3	200	1	400	.05	1	.001	On	Off
7	1	1	200	1	400	.05	1	.001	On	Off
8	1	.3	200	1	400	.05	1	.001	On	Off
9	1	.1	200	1	400	.05	1	.001	On	Off
10	.1	.3	200	1	400	.05	1	.001	On	Off
11	10	.3	200	1	400	.05	1	.001	On	On
12	1	1	200	1	400	.05	1	.001	On	On
13	1	.3	200	1	400	.05	1	.001	On	On
14	1	.1	200	1	400	.05	1	.001	On	On
15	.1	.3	200	1	400	.05	1	.001	On	On

Table 2.1: **Simulation parameters for all the numerical experiments.** N_m is the number of wave modes both in δB_x and δB_y . N_c is the number of control points. N_p is the number of test particles. R_w is the radius of the sliding window for the numerical experiment for calculating the $D_{\mu\mu}$. N_b is the number of bins in the μ space $([-1, 1])$ used to calculate $D_{\mu\mu}$.

According to Roberts (2012), the phase angles β_n and θ_n are chosen such that the variance σ_b^2 is a minimum. This is called an "optimization". In practice, one needs to define the "control" points, which are a set of points, $\{z_i | i = 0, 1, \dots, N_z\}$. They will be used to evaluate σ_b^2 , the variance of $b(z)$ in

Equation (2.3) during the optimization. As a result of the optimization, we also find that the variance of the B_x and B_y components ($\sigma_{B_x}^2$ and $\sigma_{B_y}^2$) of the magnetic field also decrease. This is because the chosen control points do not cover a large enough range in z to maintain the variance of the B_x and B_y components of the magnetic fields. To clarify this point, consider a simpler case of just two wave modes, such that

$$B_x = A_{k_1} \sin(k_1 z + \beta_1) + A_{k_2} \sin(k_2 z + \beta_2)$$

The variance is given by $\sigma_{B_x}^2 = \langle B_x^2 \rangle = \frac{1}{T} \int_0^T B_x(z) dz$, and T is the range of the control points in z . Then we have

$$\begin{aligned} \sigma_{B_x}^2 &= A_{k_1}^2 \langle \sin^2(k_1 z + \beta_1) \rangle + A_{k_2}^2 \langle \sin^2(k_2 z + \beta_2) \rangle + 2A_{k_1}A_{k_2} \langle \sin(k_1 z + \beta_1) \sin(k_2 z + \beta_2) \rangle \\ &= A_{k_1}^2 \langle \sin^2(k_1 z + \beta_1) \rangle + A_{k_2}^2 \langle \sin^2(k_2 z + \beta_2) \rangle \\ &\quad - A_{k_1}A_{k_2} (\langle \sin[(k_1 + k_2)z + \beta_1 + \beta_2] \rangle - \langle \sin[(k_1 - k_2)z + \beta_1 - \beta_2] \rangle) \end{aligned}$$

The first and second term will average to $1/2$ given a large enough integration range in z , say $T = \frac{2\pi}{k_1 * k_2}$. And the third and the fourth term will only average to zero given the integration range in z is as large as $T' = \frac{2\pi}{(k_1 + k_2) * |k_1 - k_2|}$.

In our more general case, the range of z that is used in the optimization is $R_z = \frac{2\pi}{k_{min}}$. And the smallest space between two points in the set of control points used for the optimization, is $d_z = \frac{2\pi}{k_{max}}$. This is a compromise between the optimization and the computational efficiency. However, this range in z is not large enough to make all the cross terms, such as the third

and fourth terms in the simple example given above, average to zero, as expected mathematically. Nevertheless, the optimization still leads to smaller magnitude fluctuations and relatively large fluctuations in the components of $\delta\mathbf{B}$.

Moreover, we can compensate for this effect by multiplying both amplitudes of the B_x and B_y components by a new factor, α , to raise the total variance back to the same level as before the optimization. This gives:

$$\sigma^2(\delta B_x)_{before} + \sigma^2(\delta B_y)_{before} = \alpha^2 [\sigma^2(\delta B_x)_{after} + \sigma^2(\delta B_y)_{after}] \quad (2.6)$$

Here the subscript "before" means before the optimization, and "after" means after the optimization. We refer to this procedure as 'Scale-up' in the numerical experiment. We perform simulations both using this scale-up procedure, as well as without it to study its effect on our results.

To set up the magnetic field described by Equations 2.1-2.5, we use a maximum wave length $\lambda_{max} = 100L_c$ and a minimum wave length $\lambda_{min} = .01L_c$ for the linear modes. We use 20000 points along the z axis over the range of $[-50L_c, 50L_c]$. The correlation length is taken to be .01 AU as observed in the near Earth solar wind (Matthaeus & Goldstein, 1982; Matthaeus et al, 2005; Wicks et al, 2009, 2010). We have simulated 5 different combinations of particle energies and variances of the magnetic field strength. For each combination, we tested three situations: 1) without optimizations; 2) with optimizations; and 3) with optimizations and scale-up procedure (described above). These are listed as in Table 2.1 We note that in each case, the mean-

free path of the particles is much less than the box size.

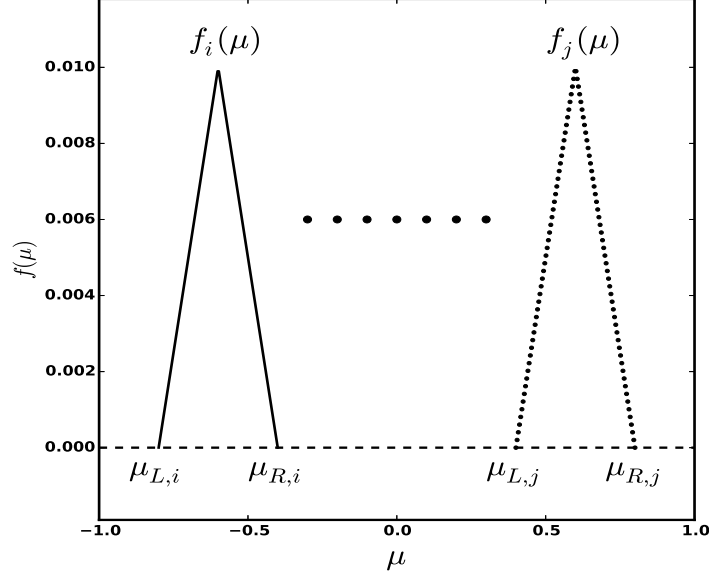


Figure 2.1: A schematic plot of sliding windows used in the numerical experiments for calculating the scattering coefficients. The unit in the y axis is arbitrary. Each sliding window (e.g. the i^{th} window) has a left boundary ($\mu_{L,i}$) and a right boundary ($\mu_{R,i}$). We calculate the scattering coefficients $D_{\mu\mu}$ for each window, and by sliding the windows through the μ space, we have an estimate of the $D_{\mu\mu}$ over the range of μ . The width of the window has to be wide enough for the diffusion process described in the equation (2.8).

2.3 Tracking the Energetic charged particles

A charged particle moving in a magnetic field, such as that described in the previous section, will move according to the Lorentz force equation given by:

$$\frac{d\mathbf{v}}{dt} = \frac{q}{\gamma mc} \mathbf{v} \times \mathbf{B} \quad (2.7)$$

where q is the charge, $\gamma = 1/\sqrt{1 - (v/c)^2}$ the Lorentz factor, m the mass, \mathbf{v} the velocity, and c the speed of light. We solve this set of equations by using the 8th order adaptive step-size Runge-Kutta method to update the particle's velocity and position at each time step (Hairer et al., 1993). A comparison of the performance of the numerical integrator with the 5th order adaptive step-size Runge-Kutta method and the Bulirsch-Stoer method is shown in the Appendix. We record the particle's motion at the step size of $\Delta t = 0.001\Omega^{-1}$ to resolve the short enough time scale required for scattering calculations. And for the highest energy particles (10GeV), the energy is well conserved by this very high order numerical integration method up to at least $1000\Omega^{-1}$ in our test, which is longer than all the cases in our simulations. We choose three energies for the charged particles for calculations: 10 GeV, 1GeV and 100 MeV. Thus, our approach is also suitable for cosmic-ray transport in the interstellar medium.

2.4 Determining the pitch-angle diffusion coefficient

In order to determine $D_{\mu\mu}$, the pitch-angle diffusion coefficient, we use a method similar to that proposed by Kaiser et al (1978). The approach is based on the numerical integration of motion of a very large number of test particles in the synthetic magnetic field described in the previous section. It is assumed

that the collection of the particles, described by a distribution function, f , obeys the pitch-angle diffusion equation given by:

$$\frac{\partial f}{\partial t} = \frac{\partial}{\partial \mu} [D_{\mu\mu} \frac{\partial f}{\partial \mu}] + S \quad (2.8)$$

where μ is the cosine of the pitch angle, $D_{\mu\mu}$ is the diffusion coefficient and $S = S(\mu, t)$ is in general the source function to be supplied. The steady-state solution to Equation 2.8 for absorbing boundary conditions, $f(\mu_L) = f(\mu_R) = 0$, where $\mu_L < \mu < \mu_R$ is the region of the solution, and a point source of the particles at μ_0 of the form $S = S_0 \delta(\mu - \mu_0)$ where μ_0 is the injection μ , gives an estimate of $D_{\mu\mu}$ on $[\mu_L, \mu_R]$ (Kaiser et al, 1978):

$$D_{\mu\mu} = \begin{cases} -\frac{J_L}{df/d\mu}, & \mu_L < \mu_0 \\ -\frac{J_R}{df/d\mu}, & \mu_0 < \mu_R \end{cases} \quad (2.9)$$

where J_L and J_R are the flux of particles crossing the left and right boundaries, μ_L and μ_R respectively.

Because of the $df/d\mu$ factor in the denominator of Equation 2.9, this process leads to a rather "noisy", or uncertain determination of $D_{\mu\mu}$. To reduce the noise, and aiming at a more accurate calculation of f , we use a "sliding window" approach, where the entire μ range from -1 to 1 is subdivided into 2000 smaller region that overlap one another. $D_{\mu\mu}$ is determined in each smaller region and averaged at each bin over all the sliding windows given by

$$D_{\mu\mu}(\mu) = \frac{1}{N_w} \sum_{i=1}^{N_w} D_{\mu\mu,i}(\mu) \quad (2.10)$$

where N_w is the number of sliding-windowed values each bin accumulates. This gives a much smoother and statistically significant $D_{\mu\mu}$. For each bin

400 particles are used to determine $D_{\mu\mu}$ from Equation 2.9. We count how many (N_L) particles leave from the left boundary in μ and how many (N_R) leave from the right boundary in μ in each bin, and then we have

$$J_L = N_L/\Delta t \quad (2.11)$$

$$J_R = N_R/\Delta t \quad (2.12)$$

where Δt is one time step in the simulation. And also we have that for the i^{th} bin in μ space,

$$f(\mu_i) = \frac{N(\mu_i)}{\Delta\mu} \quad (2.13)$$

We apply a linear regression on $f(\mu)$ over μ to calculate $df/d\mu$. By fitting to the above solution in f , μ and J , we have an estimate of the scattering coefficients over the one sliding window of $[\mu_L, \mu_R]$ in the μ space. The width of each sliding window is .05, and the bin size (to compute $f(\mu)$ within each window) in the μ space is .001. We slide the window through $[-1, 1]$ to cover the whole μ space, with a sliding distance of .009 in the μ space until out of its range. This procedure gives $D_{\mu\mu}$ as a function of the entire region of μ from -1 to 1 . Note that for each window, we use 400 particles per realization and 48 realizations for a total of 400×48 total particles.

2.5 Results

Our results of the calculated pitch-angle diffusion coefficients from the test cases in Table 2.1 are shown in the plots in Figure 2.2 and 2.3. The Quasi-

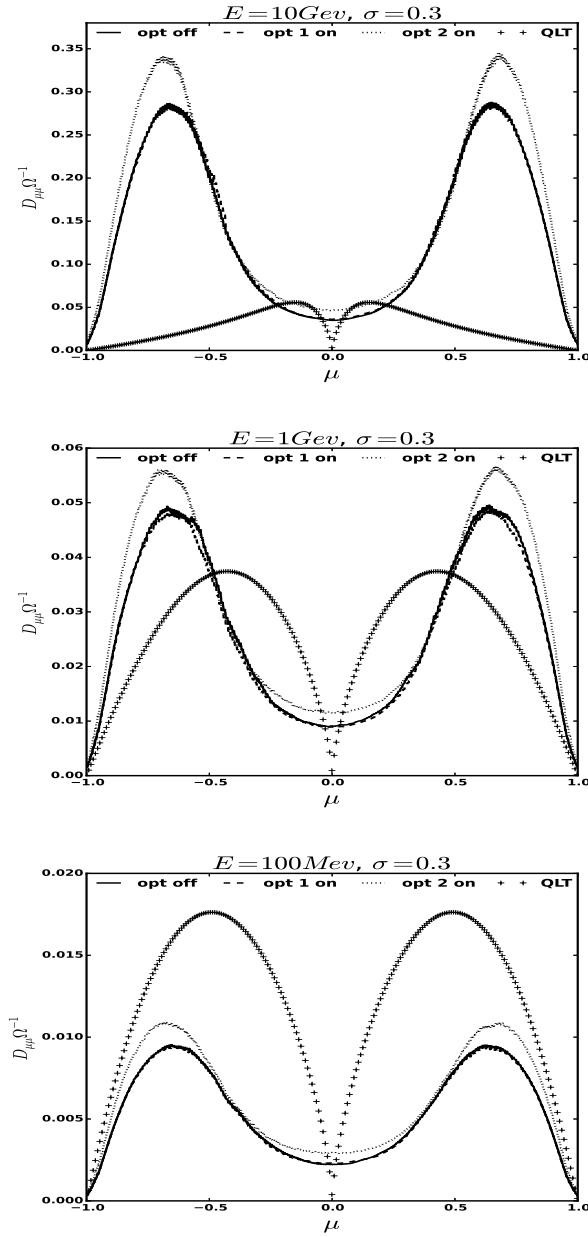


Figure 2.2: $D_{\mu\mu}$ calculated for particles with different energies with and without field optimizations. a) Cases 1, 6, 11 in Table 2.1, b) cases 3, 8, 13 in Table 2.1, c) cases 5, 10, 15 in Table 2.1. "OPT OFF" means there is no optimization, and the data are marked as solid lines. "OPT 1 ON" means Optimization is applied, but without scale up procedures. The data in this case are marked as dashed lines. "OPT 2 ON" means both optimization and scale-up are applied to the fields. "QLT" means the Quasi-Linear Theory estimates. And the data in this final case are marked as dotted lines.

Linear Theory estimate is plotted in lines marked by cross in each plot for reference. Notice that in those test cases that the magnetic field is strongly turbulent, the deviation from the QLT estimate is significant, but when the field is weakly turbulent, the QLT estimate predicts better results.

Figure 2.2 shows how the $D_{\mu\mu}$ changes if we change the energy of the charged particles from 100 MeV up to 10 GeV. For each combination of the charged particle energy and the turbulent field strength, we tested three situations: 1) the normal slab turbulence; 2) the normal slab turbulent magnetic field with the nearly constant magnitude; and 3) the normal slab turbulent magnetic field with the nearly constant magnitude plus the variance-conserving adjustment. From all the three panels in Figure 2.2 we could see there is little difference between the situations without any optimizations and situations with only optimizations. However, there is a significant overall increase in $D_{\mu\mu}$ if we apply the scale-up in all three panels. Figure 2.3 shows the results for the cases when we keep charged particle energy the same and change the turbulent field strengths. We also tested the three situations in each panel of the Figure 2.3 as in Figure 2.2. We find similar effects in all the situations as in Figure 2.2.

One possible reason that the optimization has no effect on the scattering might be because the optimization is highly related to the control points that are chosen and used to perform the optimization itself. In our simulation, we chose 20000 points in the range $[-50L_c, 50L_c]$ along the z-axis, which means the

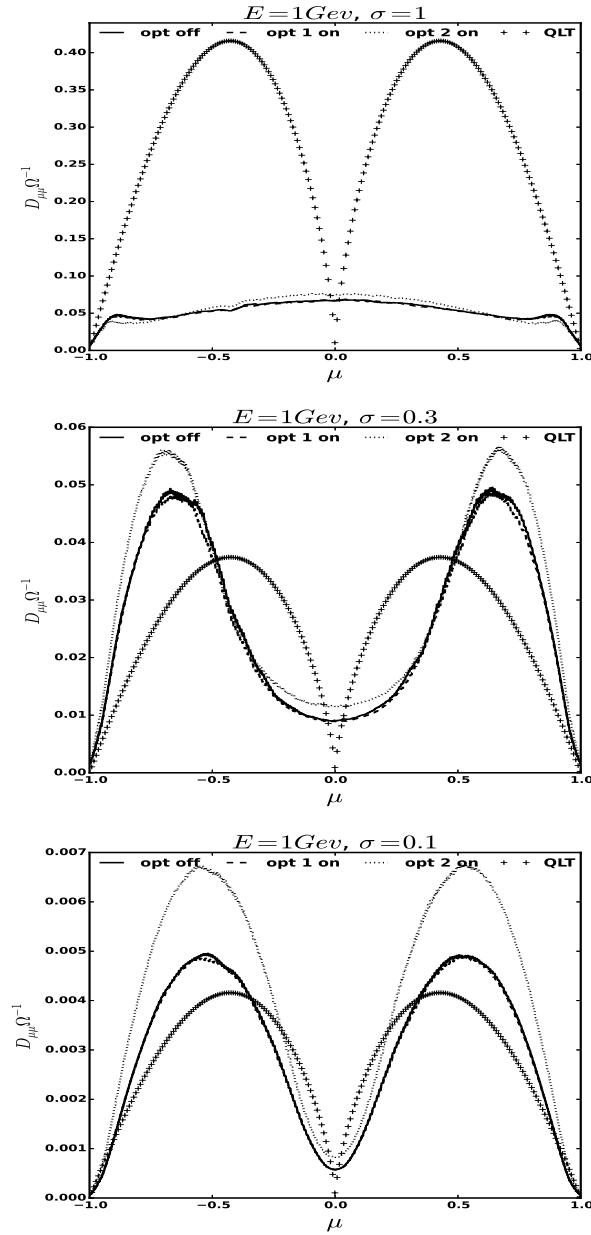


Figure 2.3: $D_{\mu\mu}$ calculated for particles with different energies with and without field optimizations. a) Cases 2, 7, 12 in Table 2.1, b) cases 3, 8, 13 in Table 2.1, c) cases 4, 9, 14 in Table 2.1. "OPT OFF" means there is no optimization, and the data are marked as solid lines. "OPT 1 ON" means Optimization is applied, but without scale up procedures. The data in this case are marked as dashed lines. "OPT 2 ON" means both optimization and scale-up are applied to the fields. "QLT" means the Quasi-Linear Theory estimates. And the data in this final case are marked as dotted lines.

smallest wavelength in our sampling control point set is .01. And this happens to be the shortest wavelength of the linear modes of the magnetic turbulence we generated, hence is enough for the purpose of the optimization. However, when we perform test particle simulations, the high precision particle tracker algorithm will advance in such a tiny time step that the spacial advancement of a particle might be smaller than the smallest wavelength of the linear mode of the field, or the shortest wavelength of our sampling control points used for optimizations. It is as if the test particle simulation is advancing on a dense and compact mesh while the optimization is performed on a relatively loose and sparse one. Therefore the effect of the optimization might not be significant enough. However, due to the nonlinearity of the scattering system, it is only possible to make the mesh grid of the control points approach the density and compactness of the set of the positions many particles would travel in the same region, which has infinite points theoretically. This also explains the difficulty in practice to extend the same algorithm to the higher dimension magnetic turbulence models. Nonetheless, in our experiments, there is no significant effect observed on the scattering from the optimization.

Another interesting result is the effect of the scale-up procedures. In all cases, it shows a significant increase in the scattering. This again is related to the fact that we could only use limited number of control points. Therefore, although applying the scale-up procedure will not change the variance of the turbulent field over the same set of the control points, the actual effect

is to increase the variance if we include all the possible points in the range $[-50L_c, 50L_c]$ along the z -axis. According to the Quasilinear theory (Jokipii, 1966), it is apparent that the scattering would be enhanced in more turbulent fields while keeping other conditions the same. Therefore one should not include the scale-up procedure in the optimization in the future numerical experiments.

It should be noticed that through our numerical simulations we thought about the possible effect of different optimization algorithms. Mathematically, one could choose a brute force method, or some other methods such as the gradient descendant method or stochastic gradient descendant method to find the optimized set of β_n and θ_n to minimize the variance of the magnitude of the magnetic field. In this case, the latter ones have the merit of computational efficiency and convenience of coding in practice. However, since the multi-variable nature of the optimization problem in β_n and θ_n , the brute force method is very reliable on finding out the globally optimized solutions, while the more advanced methods might stop the search at a local minimum, which is very hard to diagnose. It is also possible to tune the code of the brute force method to achieve such a high efficiency both in the memory usage and the time complexity that is enough to run all the simulations in our practice.

2.6 Conclusion

In this chapter we used the sliding-window numerical experiments to calculate the charged particle scattering coefficients as a function over μ , the cosine of the particle's pitch angle. We tested results for different combinations of the charged particle energies and turbulent magnetic field strengths. For each combination, we tested three situations: 1) without optimizations, 2) with optimizations and 3) with optimizations and scale-ups. We found that there is no effect on particle's scattering over the pitch angle space by only applying the optimization to the turbulent magnetic fields. And we also found that the sliding-window numerical experiment is an efficient numerical method to determine charged particle scattering in the turbulent magnetic fields. A future work would be applying this optimization in the three dimensional isotropic turbulent magnetic field models while performing both the numerical experiment on the scattering and the ones on the diffusion for charged particles to observe the effects of the optimizations.

Chapter 3

Global Anisotropy

A successful synthesis method incorporates all the features proposed by different MHD turbulence models including a) the zero divergence of the magnetic field, b) anisotropic power spectra of the magnetic fields over the wave number space and c) the scale dependence of the anisotropy. How the restraints b and c would affect the charged particle transport is of interest. We define the global anisotropy such that the type of MHD turbulence model satisfies conditions a) and b), and define the local anisotropy such that all the conditions a), b) and c) are satisfied. On the other hand, global anisotropy means we would only specify one power spectrum anisotropy function for all the components at different wave numbers (see section 2 for the details), while the local anisotropy means the power spectrum anisotropy function will also be different at different scales (the details will be given in the next chapter).

In this chapter we compare the influence of the globally anisotropic turbulence, on the transport of charged energetic particles, with previous turbulence

models. We consider protons with energy from $1\text{MeV} \sim 1\text{GeV}$ traveling in the solar wind. Section 2 describes the method used to generate the turbulent magnetic field. Section 3 lists the parameters used in simulation. Section 4 shows the results and discussion and, section 5 is conclusion. And in the next chapter we will add in the scale dependence of the anisotropy to the turbulence model and observe the consequences.

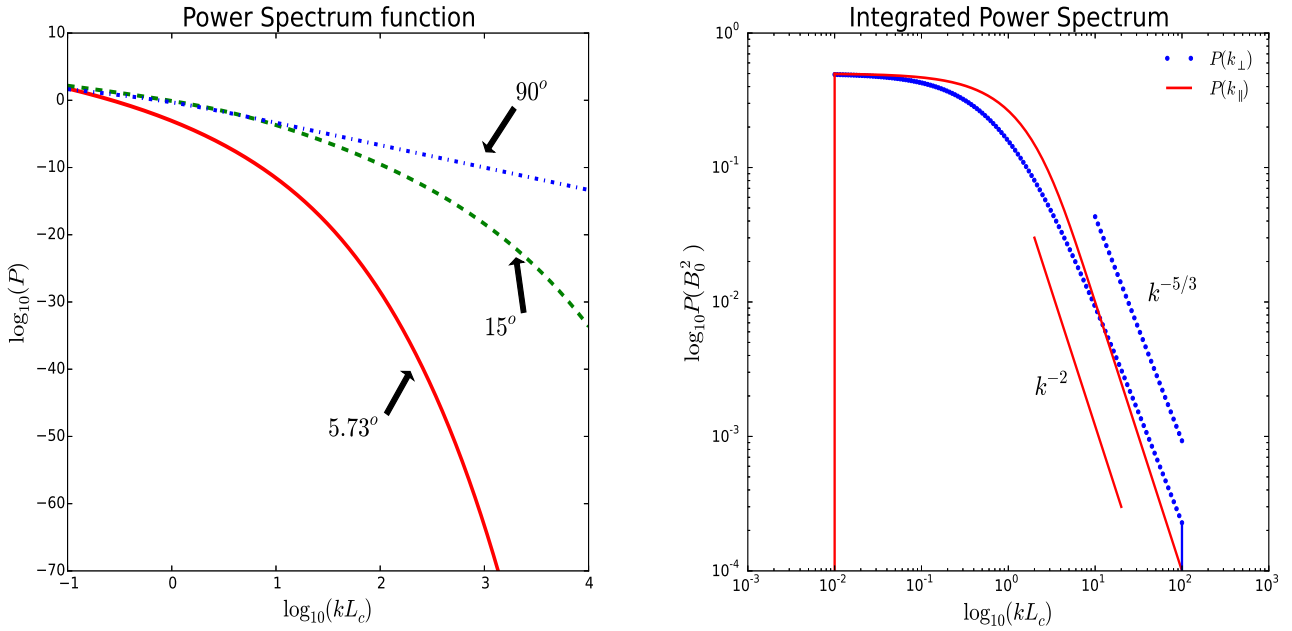


Figure 3.1: **Power spectra of random magnetic fluctuations versus k_\perp and k_\parallel . The left panel shows the power spectrum as in equation (3.7). It is the function P of wave numbers perpendicular and parallel to the mean field with azimuthal symmetry. The colors indicate large value as red and small as blue. The solid lines are the contours of the isotropic power spectrum for comparison. All the values are normalized to the scale ranges from 0 to 1. The right panel shows the integration of equation (3.7) over k_\parallel in blue or over k_\perp in red, which is then only a function of k_\perp or k_\parallel .**

3.1 Synthesis of the magnetic fields

The static magnetic field that is synthesized uses a method similar to that used by Giacalone & Jokipii (1999) (hereafter referred as GJ99) for isotropic and composite turbulence. Our synthesized field is given by

$$\mathbf{B} = B_0 \hat{\mathbf{z}} + \delta \mathbf{B}(x, y, z) \quad (3.1)$$

$$\delta \mathbf{B}(x, y, z) = \sum_{n=1}^{N_m} A(k_n) \hat{\xi}_n \exp(ik_n z'_n + i\beta_n) \quad (3.2)$$

$$\hat{\xi}_n = \cos \alpha_n \hat{\mathbf{x}}'_n + i \sin \alpha_n \hat{\mathbf{y}}'_n \quad (3.3)$$

$$\begin{pmatrix} \mathbf{x}' \\ \mathbf{y}' \\ \mathbf{z}' \end{pmatrix} = \begin{pmatrix} \cos \theta_n \cos \phi_n & \cos \theta_n \sin \phi_n & -\sin \theta_n \\ -\sin \phi_n & \cos \phi_n & 0 \\ \sin \theta_n \cos \phi_n & \sin \theta_n \sin \phi_n & \cos \theta_n \end{pmatrix} \begin{pmatrix} \mathbf{x} \\ \mathbf{y} \\ \mathbf{z} \end{pmatrix} \quad (3.4)$$

$$A^2(\mathbf{k}_n) = \frac{P(k_n, \theta_n) \Delta k^3}{\sum P(k_n, \theta_n) \Delta k^3} \quad (3.5)$$

$$P(k_n, \theta_n) = \frac{\sigma_B^2 L^3 \exp\{-(k_n L)^{1/3} \sin \theta_n / |\cos \theta_n|^{2/3}\}}{6\pi (k_n L |\cos \theta_n|)^{5/3} (1 + k_n L |\cos \theta_n|)^{5/3}} \quad (3.6)$$

Where for wave mode n , $A(k_n)$ is the amplitude of the wave mode k_n , α_n represents polarization, β_n phase, θ_n and ϕ_n the direction of propagation with respect to the polar axis z_0 , and $P(k_n, \theta_n)$ is the power spectrum function.

Here we use the power spectrum function at wave numbers k_\perp and k_\parallel with $P(k_\perp, k_\parallel) \sim (k_\perp)^{-10/3} f(k_\parallel/k_\perp^{2/3})$, where k_\parallel is the parallel wave number and, k_\perp the perpendicular wave vector (Goldreich & Sridhar, 1995). Notice that this definition is only valid for both wave numbers in the turbulence inertial range. For the function $f(L^{1/3} k_\parallel / (k_\perp)^{2/3})$, which dictates the critical

balance between k_{\parallel} and k_{\perp} in the local reference frame but is undetermined in Goldreich & Sridhar (1995), we take the exponential form proposed in Cho et al. (2002). The spectrum function used in the simulation is listed as follows

$$P_{ii}(k_{\perp}, k_{\parallel}) = P(k_{\perp}, k_{\parallel}) = \frac{\sigma_B^2 L^3 \exp\{-L^{1/3}|k_{\parallel}|/(k_{\perp})^{2/3}\}}{6\pi(k_{\perp}L)^{5/3}(1+k_{\perp}L)^{5/3}} \quad (3.7)$$

Where $P_{ii}(k_{\perp}, k_{\parallel})$ (here $i = x, y, z$) is the diagonal components of the magnetic field power spectra tensor P_{ij} , σ_B^2 is the variance of the magnetic field magnitude and L is the turbulence injection length. Notice that we use a form that is asymptotic to the form of $P(k_{\perp}, k_{\parallel}) \sim (k_{\perp})^{-10/3} f(k_{\parallel}/k_{\perp}^{2/3})$ in the inertial range and a constant in small wave numbers in the energy containing range. Figure 3.1 shows how the shape of the above spectrum function (log values) changes with wave numbers $(k_{\parallel}, k_{\perp})$ in the Fourier space. In the left panel, when the wave numbers are small (at large scales), the spectrum becomes isotropic. As both the wave numbers $(k_{\parallel}, k_{\perp})$ increase (at small scales), the spectrum becomes elongated along k_{\perp} . This anisotropy corresponds to what would be expected in Goldreich-Sridhar type spectrum. In the right panel, the power spectrum is integrated over k_{\parallel} to be a function only of k_{\perp} . This is the power spectrum with index $-5/3$, as the Kolmogorov power spectrum.

3.2 Numerical method and parameters

Since the energetic particles, such as in the solar wind, have a much lower energy density than that of the thermal particles or the magnetic field we

may use a test particle simulation. The Lorentz force governs the motion of charged particles:

$$\frac{d\mathbf{v}}{dt} = \frac{q}{\gamma mc} \mathbf{v} \times \mathbf{B} \quad (3.8)$$

where q is the charge, $\gamma = 1/\sqrt{1 - (v/c)^2}$ the Lorentz factor, m the mass, \mathbf{v} the velocity, and c the speed of light, and the magnetic field is described as in Section 2.

We solve this equation using a fourth order, adaptive-step Runge-Kutta method (Press et al., 1986) such that each step size is adjusted to preserve the given error tolerance. For each case listed in table 3.1, we used 2400 particles and 48 realizations of magnetic field with different sets of random wave modes as mentioned in the last section. And for each realization there are 50 particles that have the same initial speed and position but are in different directions isotropically.

The transport coefficients are calculated in the same way as in GJ99 by fitting the solution to a finite absorbing boundary diffusion problem. We assume a point source of particles released at time $t = 0$, and that the particle spatial distribution $f(x, t)$ as a function of time along the axis x obeys the 1D diffusion equation. We also assume that the turbulence is spatially homogeneous and that the diffusion coefficient κ_{xx} is constant over time. And there are two absorbing boundaries at $x = \pm L$.

$$\left\{ \begin{array}{l} \frac{\partial f(x, t)}{\partial t} - \kappa_{xx} \frac{\partial^2 f(x, t)}{\partial x^2} = 0 \\ -L < x < L, f(x, 0) = N_0 \delta(x), \end{array} \right. \quad (3.9)$$

where $|x| = L$ is the absorbing boundary, $f(x, t)$ is the distribution function of particles, and N_0 is the total initial number of particles. We first find the theoretical solution of the above equations and then the total number of remaining particles is

$$N(t) = \int_{-L}^L f(x, t) dx = \frac{4N_0}{\pi} \sum_{n=1}^{\infty} \frac{(-1)^{n+1}}{2n-1} e^{-k_{xx} \left[\frac{(2n-1)\pi}{2L} \right]^2 t} \quad (3.10)$$

In each case of the numerical simulations listed in Table 3.1, the remaining particles are counted and saved at each time step. The transport coefficient κ_{xx} is estimated by the least square fitting to the above formulas with observed N at t , and known parameters N_0 and L .

Simulation Results										
Case	Energy	r_g	σ^2	L_c	L_c/r_g	λ_{min}/r_g	λ_{max}/r_g	κ_{\perp}	κ_{\parallel}	$\kappa_{\perp}/\kappa_{\parallel}$
-	MeV	10^{-3} AU	AU	10^{-2} AU	1	1	1	$10^{18} \frac{cm^2}{s}$	$10^{20} \frac{cm^2}{s}$	0.01
1	1.0	0.193	1.0	1.0	51.9	0.519	5190	3.22	1.04	3.1
2	3.16	0.343	1.0	1.0	29.2	0.2917	2917	6.43	2.20	2.9
3	10.0	0.611	1.0	1.0	16.4	0.1637	1637	11.4	4.79	2.4
4	31.6	1.09	1.0	1.0	9.15	0.0915	915.4	27.1	12.5	2.2
5	100	1.98	1.0	1.0	5.06	0.0506	505.8	53.5	27.2	2.0
6	316	3.70	1.0	1.0	2.70	0.0270	270.0	118	67.2	1.8
7	1000	7.59	1.0	1.0	1.33	0.0133	132.6	234	163	1.4
8	10000	48.6	1.0	1.0	0.21	0.0021	20.58	1721	606	2.8
9	10000	48.6	1.0	1.0	0.21	0.0021	20.58	1198	766	1.6
9	31.6	1.09	0.5	1.0	9.15	0.0915	915.4	16.8	25.7	0.65
10	31.6	1.09	0.3	1.0	9.15	0.0915	915.4	10.4	72.9	0.14
11	31.6	1.09	0.1	1.0	9.15	0.0915	915.4	8.69	122	0.07
12	31.6	1.09	0.05	1.0	9.15	0.0915	915.4	5.93	217	0.03
13	31.6	1.09	0.01	1.0	9.15	0.0915	915.4	1.46	346	0.004

Table 3.1: The results are from the correspondent cases using Goldreich Sridhar type turbulence spectrum as equation (3.7).

Listed in Table 3.1 are simulation cases and related parameters. The column with Energy in MeV gives the energy of test particles. r_g is the gyro-radius. σ^2 gives the variance of the synthesized magnetic field normalized to its mean value. L_c is the correlation length of the magnetic turbulence. λ_{min} and λ_{max} define the range of the wave length of the Fourier modes we used

in the synthesis of the magnetic field. They are the same as in GJ99 for the convenience of comparison with isotropic and composite cases. Figure 3.1 shows the power spectrum generated by equation (4.12). The variance of the turbulence magnetic field is 1.0 in case 1 to 7 and varies in case 4 and 8 to 12.

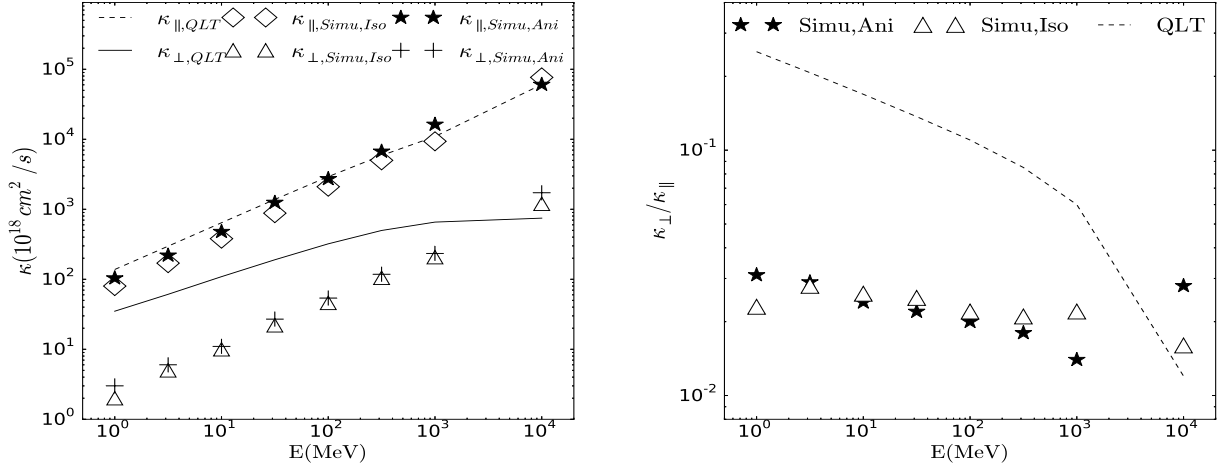


Figure 3.2: The left panel shows perpendicular and parallel transport coefficients in both GS type and isotropic turbulence spectrum, as a function of the particle's energy. The stars and crosses, κ_{\perp} and κ_{\parallel} respectively, are values in Table 3.1. The diamonds and triangles are simulation results from cases with the isotropic turbulence power spectrum as in Giacalone & Jokipii (1999). The diamond is the parallel diffusion coefficient while the triangle the perpendicular coefficient. The dashed line and solid line are the coefficients calculated by equations 3.11 and 3.13 respectively. The right panel shows their ratio as the function of proton energy. Stars are $\kappa_{\perp}/\kappa_{\parallel}$'s from Table 3.1. And triangles represent simulation results with isotropic turbulence model, and the dashed line is from equations (3.11) and (3.13) using GS type power spectrum. All the results as according to the cases 1 to 7 in Table 3.1.

3.3 Results

Figure 3.2 shows how the κ_{\perp} , κ_{\parallel} (left panel) and $\kappa_{\perp}/\kappa_{\parallel}$ vary with particle's energy, as in case 1 to 9 in table 1. Notice that case 9 is calculated in the isotropic model. Figure 3.3 shows how the κ_{\perp} , κ_{\parallel} (left panel) and $\kappa_{\perp}/\kappa_{\parallel}$ vary with magnetic field variance, as in case 4 and 8-12 in table 1. Both coefficients increase with particle's energy, and the magnitude of these two coefficients are close to those calculated in GJ99 from isotropic (and composite) turbulence spectrum. Our result also agrees well with the UNLT (Unified Non-Linear Transport) theory (Shalchi & Hussein, 2015), with the parameter in the UNLT model $a^2 \sim 1$. Also according to Quasi-Linear Theory, the perpendicular coefficient is (Jokipii, 1966)

$$\begin{aligned}\kappa_{\perp} &= \frac{1}{2} \int_0^1 d\mu \left\{ \frac{\mu v}{B_0^2} P_{\perp}(k_{\perp} = 0) + \frac{(1 - \mu^2)v}{2|\mu|B_0^2} P_{\parallel}(k_{\parallel} = \frac{\Omega_0}{\mu v}) \right\} \\ &\cong \frac{v L_c \sigma_B^2}{6 B_0^2}\end{aligned}\quad (3.11)$$

A quick estimate using the above equation would tell us the dominant components that affect the charge particle perpendicular transport in both isotropic and Goldreich-Sridhar type turbulence are the low wave number components of the turbulent magnetic fields. Also note that this estimation is similar to the result from the UNLT theory where two important parameters for the perpendicular diffusion coefficient are the parallel mean free path l_{\parallel} and the Kubo number. In the above equation, we could regard the l_{\parallel} as a

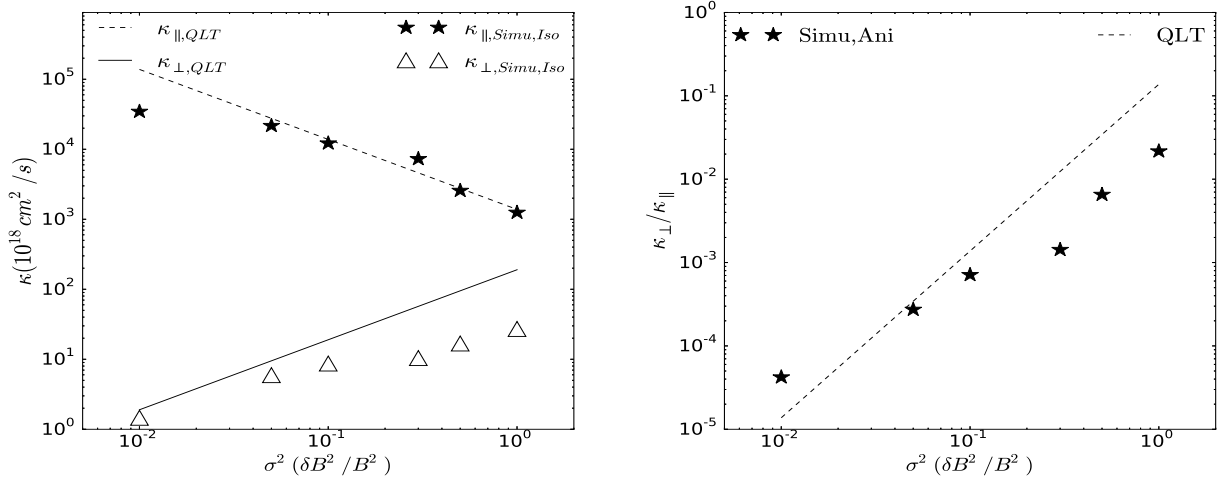


Figure 3.3: In the left panel, stars and triangles show perpendicular and parallel transport coefficients from Table 3.1, as a function of variance of the field strength, while the test particles have a fixed energy of 31.6 MeV. Similar to Fig.3.2, The dashed line and solid line are estimated from equations (3.11) and (3.13) for perpendicular and parallel diffusion coefficients respectively. In the right panel, stars show the ratio of κ_{\perp} to κ_{\parallel} from Table 3.1 varies with the variance of the field strength while the dashed line represent also the calculation from equations (3.11) and (3.13). The results are according to the case 4 and 8-12 in Table 3.1.

function of vLc and the Kubo number in this case is σ_B^2 / B_0^2 . In the simulation however, it is expected to be a little different from the estimate by the Quasi-Linear Theory. This could be due to the fact that the longest wave length in the simulation is $100Lc$, which corresponds to the wavenumber of $k \sim 10^{-2}$, instead of an infinite long wave theoretically. In the parallel diffusion case, the scattering rate and diffusion coefficient could be calculated by (Jokipii, 1966; Earl, 1974; Luhmann, 1976)

$$\begin{aligned}
\nu &= \frac{2D_{\mu\mu}}{1-\mu^2} = \frac{\pi}{2}\Omega_0 \frac{k_{res}P_{\perp}(k_{res})}{B_0^2} \\
&= \frac{\pi}{3}\Omega_0 \frac{\sigma_B^2}{B_0^2} \frac{\frac{\Omega_0 L_c}{(v|\mu|)}}{(1 + \frac{\Omega_0 L_c}{v|\mu|})^{5/3}} \quad (3.12)
\end{aligned}$$

$$\begin{aligned}
\kappa_{\parallel} &= \frac{v^2}{2} \int_0^1 \frac{1-\mu^2}{\nu} d\mu \\
&= \frac{3v^3}{\pi\Omega_0^2 L_c} \frac{B_0^2}{\sigma_B^2} \int_0^1 \mu(1-\mu^2) \left(1 + \frac{\Omega_0 L_c}{v\mu}\right)^{5/3} d\mu \quad (3.13)
\end{aligned}$$

where the k_{res} is the wave number of the Fourier mode which the particle would resonate with. The values from simulation are close to the estimate from equation 3.13. The ratio $\kappa_{\perp}/\kappa_{\parallel}$, unlike in the isotropic turbulence case, decreases slightly with particle's energy, as shown in Figure 3.2. If we compare equation 3.11 to equation 3.13, we can see the ratio of transport coefficient ($\kappa_{\perp}/\kappa_{\parallel}$) is related to v^2 . However, it does not change significantly. As in the particle's energy range ($1MeV \sim 1GeV$) we tested, it is about $0.01 \sim 0.03$ for a strong turbulence ($\sigma_B^2 \sim 1$), or $\kappa_{\perp} \ll \kappa_{\parallel}$. In Figure 3.3, this ratio is even smaller for milder turbulence variances. Table 3.1 shows the result of the simulations.

Furthermore, in the Goldreich-Sridhar type turbulence, the perpendicular diffusion coefficients are larger than that in isotropic type. Since it is mainly controlled by the large scale field component, the perpendicular transport coefficients calculated in the simulation in both Goldreich-Sridhar type and isotropic case are very close to each other. This just confirms the Field Line

Random Walk theory proposed by Jokipii (1966) and Jokipii & Parker (1969) on particle's transverse motion.

Notice also that $\nu \sim (v\mu)^{2/3}\sigma_B^2$, then by Quasi-Linear Theory, it is zero at pitch angle $\theta = 90^\circ$ and would maximize at $\theta \sim 0^\circ$. Also it increases with particle's energy and the variance of magnetic turbulence. This could be related to the magnetic mirror effect induced by the fast mode wave in the turbulence, which will increase the scattering rate. While the scattering rate is important in diffusive shock acceleration, one might estimate that in turbulence model with strong fast-mode cascading, the acceleration will be enhanced.

Figure 3.3 shows how the κ_\perp , κ_\parallel (left panel) and $\kappa_\perp/\kappa_\parallel$ vary with the variance of the magnetic field, as the particle's energy is 31.6 MeV. In the left panel of figure 3.3 it shows the perpendicular transport coefficient increases as the variance of the magnetic field increases, since in this case both the scattering and field line random walk are stronger. The parallel transport coefficient is smaller, since the mean free path in this case along the field line would be smaller. Combine these two changes, the ratio of transport coefficient, $\kappa_\perp/\kappa_\parallel$, is then increasing, as the variance is increasing in the numerical simulations.

3.4 Conclusion

Using the global Goldreich&Sridhar power spectrum we constructed globally anisotropic turbulent magnetic field and performed test particle simulation to analyze particle's diffusion and the conclusions could be summarized as follows:

1. There is no significant difference on particle's diffusion between isotropic and globally anisotropic turbulence magnetic fields; Field Line Random Walk might still be the main factor of particle's diffusion;

2. The ratio $\kappa_{\perp}/\kappa_{\parallel}$ is about $0.01 \sim 0.03$ for a strong turbulence ($\sigma_B^2 \sim 1$); and

3. $\kappa_{\perp} \sim \sqrt{E}\sigma_B^2$, $\kappa_{\parallel} \sim \sqrt{E^3}(\sigma_B^2)^{-1}$.

Based on their recent numerical simulations, Hussein et al. (2015) also conclude the similarity of charged particle diffusion in isotropic and globally anisotropic magnetic turbulence using a different synthesis approach for the static magnetic field. However, the synthesized magnetic turbulence is globally anisotropic in both syntheses. However the magnetic turbulence may be locally anisotropic, in that eddies would stretch along the local mean magnetic field line in smaller scales in the turbulence inertial range. Therefore, one has to determine the local average field direction when adding the parallel and perpendicular wave components in different scales ($|k_{\parallel}| \sim k_{\perp}^{2/3}$, this result is derived from the hypothesis that the parallel cascading time is balanced with and equal to the perpendicular cascading time.). One of the difficulties arises

from the fact that when one is doing the synthesis, the average field would be changed accordingly. In the same time, the local critical balance condition ($|k_{\parallel}| \sim k_{\perp}^{2/3}$) and zero-divergence condition ($\nabla \cdot \mathbf{B} = 0$) have to be maintained at the same time. Incorporating this feature in the synthesized magnetic field and the transport of charged particles in the turbulence will be discussed in the next chapter.

Chapter 4

Local Anisotropy

The localized anisotropy GS type turbulence is supposed to have different effect on charged particle transport. In the last chapter(Sun & Jokipii, 2015) we synthesized a globally anisotropic turbulent magnetic field and found that it has similar particle transport effect compared with the isotropic field models. We propose here a general framework for a multi-scale synthesis with the scale-dependent, localized anisotropic feature incorporated. We run test particle simulations in this new field model of the two-scale algorithm to calculate the transport coefficients for charged particles with different energies. We found that the local anisotropy has the significant difference from the previous model in the effect on charged particle transport. The parallel transport coefficient (κ_{\parallel}) decreases while the perpendicular transport coefficient (κ_{\perp}) increases compared with the isotropic and globally anisotropic field models. The difference is enhanced as the local anisotropy is enhanced, and there is an order of magnitude increase in the ratio of perpendicular to

parallel transport coefficients.

4.1 Introduction

In last chapter (Sun & Jokipii, 2015) (hereafter referred as Chapter 3) we pointed out that different MHD turbulence models could have different effects on charged particle transport. We also explained that there are three methods to approach this problem: pure theoretical analysis (Jokipii, 1966; Schlickeiser & Achatz, 1993; Chandran, 2000; Yan & Lazarian, 2002; Matthaeus et al., 2003; Yan & Lazarian, 2004, 2008; Shalchi et al, 2010) etc, direct MHD turbulence simulation coupled with particle tracking codes (Beresnyak et al., 2011) etc, and finally the synthesis of different turbulent magnetic field models plus test particle simulations (Giacalone & Jokipii, 1999; Matthaeus et al., 2003; Laitinen, 2013; Hussein et al., 2015). The synthesis method has the merit of exploring much larger parameter space than the direct MHD simulation method, and also provides a possible and better way to describe the anisotropic MHD model which might lead to approachable theories on charged particle transport. We also outlined that, a successful synthesis needs to satisfy at least the following requirement: a) the field has to have zero divergence, b) the field has to be continuous, c) the field has to have the anisotropic spectrum, and d) the field has to explicitly contain the scale dependent (or local) anisotropy. However it is difficult to satisfy all the conditions at once in the same synthesis. Instead, we synthesized the globally anisotropic fields with all conditions but

d), and run test particle simulations to calculate the transport coefficients in the global anisotropy and compared with the isotropic models. We found that there is no significant difference between the global anisotropy and isotropy of the magnetic field turbulence on particle transport.

We here provide a general synthesis framework with multiple steps. We first introduce the anisotropy to the global mean field first at large scale(which is not dependent on scale or location) and then add in the small scale (large wave number) anisotropy to the local mean field of different locations. Notice the anisotropy grows as we move down to the smaller scales in the GS type MHD turbulence. And finally the power distributed among the components in the two steps are determined here by the GS power spectrum function and normalized. In section 2 we explain the first step, the large scale synthesis in this algorithm. And in section 3 we describe the algorithm for the small scale synthesis.

It is of great interest to examine the local anisotropy's effect on the charged particle transport. We therefore put test particles in the magnetic field generated by this multi-scale synthesis algorithm. We run numerical experiments to calculate the transport coefficients by the same technique as in the Chapter 3. The results are compared with the isotropic magnetic turbulence model and discussed in section 4. And finally we list our conclusions in the last section.

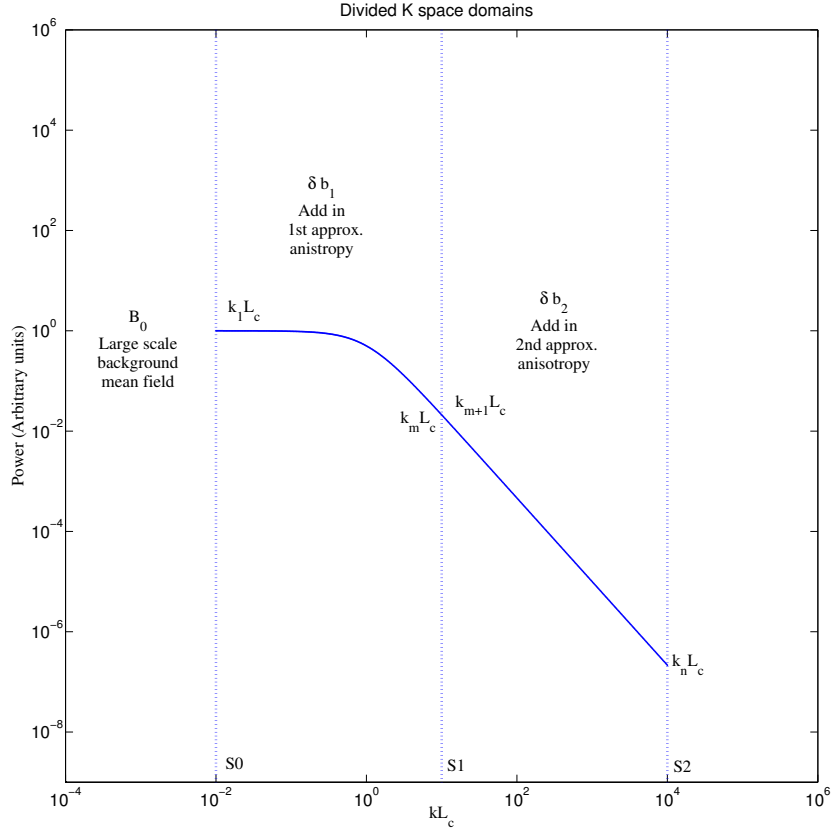


Figure 4.1: A schematic plot showing the division of the two-scale algorithm for the local anisotropy. The solid line demonstrates a power spectrum for a group of synthesis components. The $[S_0, S_1)$ (or $[K_1 L_c, K_2 L_c)$, or for k 's in $\{k_1, k_2, \dots, k_m\}$ discretely) represents the range of the wavenumber used by the large scale global synthesis, δb_1 , as in equation (5.1) and (4.33). And the $[S_1, S_2)$ (or $[K_2 L_c, K_3 L_c)$, or for k 's in $\{k_{m+1}, k_{m+2}, \dots, k_n\}$ discretely) illustrates the wavenumber range used by the small scale local synthesis, δb_2 , as well as in equation (5.1) and (4.33).

4.2 A Multi-Scale Synthesis of the Magnetic Field

Without loss of generality, we will begin the synthesis of the general non-isotropic turbulent magnetic field with the present technique used in the syn-

thesis of the isotropic turbulence (Giacalone & Jokipii, 1999), composite (Slab plus 2D) turbulence (Matthaeus et al., 2003; Bieber et al., 1996; Matthaeus et al., 1990) and the globally anisotropic turbulence such as Chapter 3 and Laitinen (2013). Consider a fully developed MHD turbulence in the steady state. The magnetic field can be defined for simplicity as an average vector component \mathbf{B}_0 plus a random vector component $\delta\mathbf{b}$

$$\mathbf{B}(\mathbf{X}) = \mathbf{B}_0(\mathbf{X}) + \delta\mathbf{b}(\mathbf{X}) \quad (4.1)$$

We can interpret \mathbf{B}_0 as the background magnetic field in the largest scale, or defined as the global mean field. The random part, $\delta\mathbf{b}$, on the other hand, could be treated as a random variable, with zero mean and certain higher order statistics, distributed in the space of interest. In the general case, if the distribution of $\delta\mathbf{b}(\mathbf{X})$ is known at each position of the space of interest, we can sample from the known probability density function (PDF). For turbulences, however, usually we would only know some low order structure functions of the PDF, like mean, variance, skewness, from theories and experiments, which is also known as Kolmogorov's 5/3 law and 4/5 law (Kolmogorov, 1941). To preserve the zero divergence property of \mathbf{B} ($\nabla \cdot \mathbf{B} = 0$), the basic building block is chosen to be the circularly polarized transverse wave mode with random polar angle α_n and phase angles β_n (Giacalone & Jokipii (1999) as

$$\delta\mathbf{b}(\mathbf{X}) = \sum_n A(k_n) \hat{\xi}_n \exp(i\mathbf{k}_n \cdot \mathbf{X} + i\beta_n) \quad (4.2)$$

$$\hat{\xi}_n = \hat{\xi}_{n1} \cos \alpha_n + i\hat{\xi}_{n2} \sin \alpha_n \quad (4.3)$$

where unit direction bases $\hat{\xi}_{n1}$, $\hat{\xi}_{n2}$ and $\hat{\xi}_{n3} = \hat{\mathbf{X}}/|\mathbf{X}|$ complete the three dimensional coordinates (see section 3 for a detailed description on how to determine the bases for different wave modes). So upon summation of wave modes of the same kind described above with different parameters (k_n , α_n , β_n , etc), the total field becomes

$$\mathbf{B}(\mathbf{X}) = \mathbf{B}_0(\mathbf{X}) + \sum_n \delta \mathbf{b}(\mathbf{X}, \mathbf{k}_n(k_n, \theta_n, \phi_n)) \quad (4.4)$$

where \mathbf{k}_n is the wavenumber vector is represented in a spherical coordinate system by its amplitude k_n , the polar angle θ_n and the azimuthal angle ϕ_n . We assume that the amplitude of each wave mode is described by Kolmogorov's 5/3 law, and that the polar and azimuthal angles are randomized for the isotropic turbulent magnetic field.

Mathematically, the above decomposition is equivalent to

$$\mathbf{B}(\mathbf{X}) = \underbrace{\langle \mathbf{B}(\mathbf{X}) \rangle_{L_1}}_{\mathbf{B}_0(\mathbf{X})} + \underbrace{(\mathbf{B}(\mathbf{X}) - \langle \mathbf{B}(\mathbf{X}) \rangle_{L_1})}_{\delta \mathbf{b}(\mathbf{X}) = \sum_n \delta \mathbf{b}(\mathbf{X}, \mathbf{k}_n)} \quad (4.5)$$

Notice that the operator $\langle \cdot \rangle_{L_1}$ is defined as $\frac{1}{L_1^3} \int_{\mathbf{L}_1^3} \cdot d\mathbf{X}$, the average of a random variable represented by \cdot with a spatial resolution L_1 of interest in different scenarios (\mathbf{L}_1^3 represents the block of size L_1). This decomposition is as straight forward mathematically as intuitive physically, because the average at the resolution L_1 physically acts as a low pass filter at the wavenumber $K_1 = 2\pi/L_1$, with all the higher ($> K_1$) wavenumber components grouped into $\delta \mathbf{b}(\mathbf{X})$.

However, it is difficult to incorporate the scale dependent features such as that in the GS theory, a small scale eddy will be elongated along the local

average field. To incorporate this feature, we need at least to specify the local average, which leads to a modified version of the above synthesis

$$\delta\mathbf{b}(\mathbf{X}) = \underbrace{\langle \delta\mathbf{b}(\mathbf{X}) \rangle_{L_2}}_{k \in [K_1, K_2]} + \underbrace{(\delta\mathbf{b}(\mathbf{X}) - \langle \delta\mathbf{b}(\mathbf{X}) \rangle_{L_2})}_{k \geq K_2} \quad (4.6)$$

Here $L_2 < L_1$ is the smaller spatial resolution, and the average sign has the similar meaning as before except that it is averaged in the resolution L_2 . We would divide the whole region by blocks with the size L_2 . Now, we can explicitly within each block determine the local average magnetic field, which is the average of the low-passed components cut off at the resolution down to L_2 and varies with spatial locations of interest from one block to another. Once we work out the local average field in each block, we place the higher wavenumber components in such a manner that will align the elongated eddy with the locally averaged fieldlines. Recall that $\delta\mathbf{b}(\mathbf{X}) = \sum_n \delta\mathbf{b}(\mathbf{X}, k_n, \theta_n, \phi_n)$, therefore the alignment is achieved by manipulate with the (θ_n, ϕ_n) for each mode.

And ideally, we can repeat the procedure and extend this decomposition to multiple resolution ranges

$$\mathbf{B}(\mathbf{X}) = \underbrace{\mathbf{B}_0(\mathbf{X})}_{k < K_1} + \underbrace{\delta\mathbf{b}_1(\mathbf{X})}_{k \in [K_1, K_2]} + \underbrace{\delta\mathbf{b}_2(\mathbf{X})}_{k \in [K_2, K_3]} + \dots \quad (4.7)$$

Notice that if we replace the K_2 with K_3 and disregard the third term we will generate the field with global anisotropy as in Chapter 3. Without loss of the generality, this process could be extended to the large enough wavenumber with multiple divisions in the K-space determined by the computation

resources and the resolution in the scenario of interest in the astrophysical environment.

For example, for charged particles with kinetic energy around 1 MeV to 10 GeV traveling in the solar wind turbulence, we just generate the field with a two-scale algorithm up to S2 as shown in Figure 4.1.

Firstly, the first term $\mathbf{B}_0(\mathbf{X})$ is the background field, usually a uniform field.

Secondly, we divide the whole region of interest into blocks correspond to the scale K_2 in the above equations.

Thirdly, the second term, $\delta\mathbf{b}_1(\mathbf{X})$, the large scale random components labeled in the wavenumber range $[K_1, K_2)$ (from S_0 to S_1 in Figure 4.1), is rewritten as

$$\delta\mathbf{b}_1(\mathbf{X}) = \sum_n \delta\mathbf{b}(\mathbf{X}, k_n, \theta_n, \phi_n) I_{[S_0, S_1)}(k_n) \quad (4.8)$$

$$I_{[S_0, S_1)}(k_n) = \begin{cases} 1 & \text{if } S_0 < k_n L_c < S_1 \\ 0 & \text{else} \end{cases} \quad (4.9)$$

Here $I_{[S_0, S_1)}(k_n)$ is the indicator function that determines the components with the wavenumber in the large scale. The amplitude of each wave mode is given by the power spectrum function in the Chapter 3 as proposed in Goldreich & Sridhar (1995). Notice that the global anisotropy is generated in the same way as in the Chapter 3, only with the stopping number in Chapter 3 replaced by the K_2 here.

Next, the third term, $\delta\mathbf{b}_2(\mathbf{X})$, in the wavenumber range $[K_2, K_3)$ (from S_1

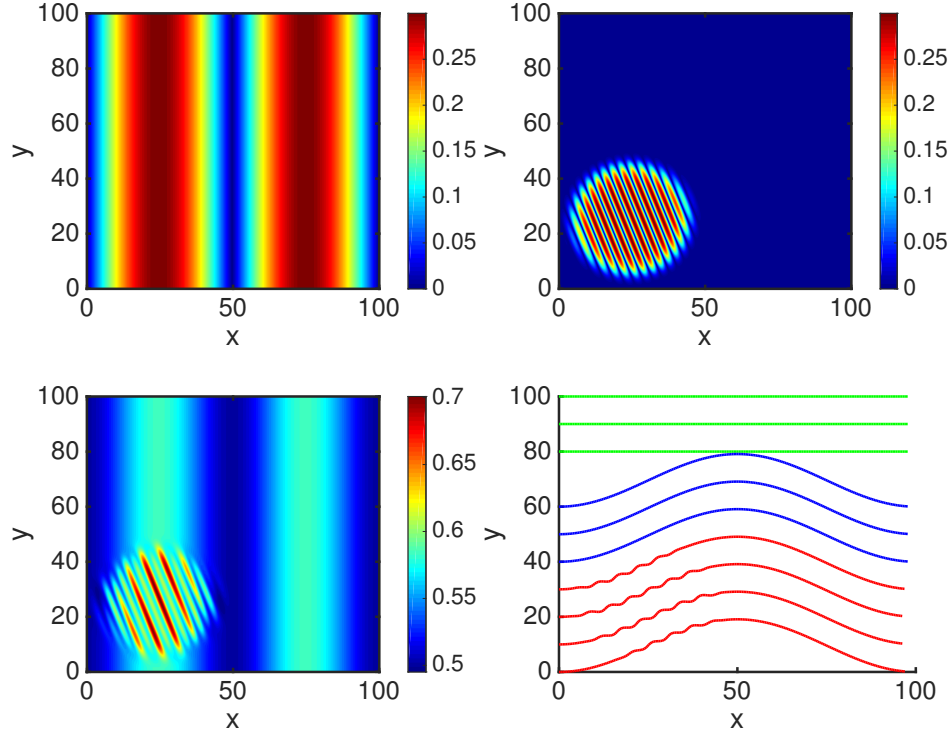


Figure 4.2: An example shows the effect and the fieldlines of the models of the mean field, the global field and the local field. *UpperLeft*: The image of the magnitude of the global mode in the x-y plane, $[0, 100]_x \times [0, 100]_y$. *UpperRight*: The image of the magnitude of the local mode in the x-y plane, only non-zero at $[0, 50]_x \times [0, 50]_y$. *BottomLeft*: The image of the magnitude of the mean field plus the global mode plus the local mode. Notice the variations due to the local mode. *BottomRight*: The green line shows the fieldline of the mean field, as represented by the equation (12). The blue lines represent . The red lines represent the fieldline of the global model plus a local component, as the example mode described in the equation (14).

to S_2 in Figure 4.1), is rewritten as

$$\delta \mathbf{b}_2(\mathbf{X}) = \sum_n \delta \mathbf{b}(\mathbf{X}, k_n, \theta_n, \phi_n) I_{[S_1, S_2]}(k_n) I_{r_i}(\mathbf{X}) \quad (4.10)$$

where $I_{[S_1, S_2]}(k_n)$ (see S1 ad S2 as shown in Figure 4.1) is the indicator

function that specifies the components used in each block (in the local scale),

$$I_{[S1, S2)}(k_n) = \begin{cases} 1 & \text{if } S1 \leq k_n L_c < S2 \\ 0 & \text{else} \end{cases} \quad (4.11)$$

and $I_{\mathbf{r}_i}(\mathbf{X})$ is used to preserve the continuity condition between blocks, where \mathbf{r}_i describes the spatial vector relative to the center of a nearest block of size L_2 . Notice that in each block that each of the $\delta\mathbf{b}_2(\mathbf{X})$ that is to be added in, the local average of the global field ($\mathbf{B}_0 + \delta\mathbf{b}_1$) has to be calculated. Once we find the local average, we will align the local component to the local average.

Finally, we need to specify the amplitude of all the synthesis components. In this chapter, this is determined by the power spectrum function proposed in Cho et al. (2002), a fitted exponential function from the MHD turbulence simulations to the general form for the spectrum function proposed in Goldreich & Sridhar (1995)

$$P(k_{\perp}, k_{\parallel}) = \frac{\sigma_B^2 L^3 \exp\{-L^{1/3}|k_{\parallel}|/(k_{\perp})^{2/3}\}}{6\pi(k_{\perp}L)^{5/3}(1+k_{\perp}L)^{5/3}} \quad (4.12)$$

This spectrum function is also used in the Chapter 3 to synthesize the global anisotropy.

Before we give the general form of the two-scale synthesis, we will begin with a simplified case for the illustration purpose. As an example shown in Figure 4.2, we illustrate in the $x - y$ plane with the size 100×100 in arbitrary units the synthesis of a simplified case with a mean field, one global component, and one local component.

Firstly, for simplicity, the mean field in the x direction through the whole plane is

$$\mathbf{B}_0 = (0.5, 0, 0) \quad (4.13)$$

Secondly, the global component, a sine mode with the wave length of 100 units and the wave vector along the x direction, takes the following form

$$\delta\mathbf{b}_1 = 0.3\hat{\mathbf{y}} \sin(0.063x) \quad (4.14)$$

Here the bold vector with a hat $\hat{\mathbf{y}}$ means the unit vector in the direction of the y-axis. Thirdly, we average the magnetic field in the left bottom area of $[0, 50]_x \times [0, 50]_y$. One then can find that the local average field in the left bottom quarter of the plane ($[0, 50]_x \times [0, 50]_y$) lies in the direction that has an angle $\theta \simeq 21^\circ$ counter-clockwise to the x-axis, or the unit vector ($\hat{\mathbf{x}} \cos \theta + \hat{\mathbf{y}} \sin \theta$).

Next, we therefore could add in the local component aligned to the local average. The magnitude of the local component is imaged in the upper right panel in Fig 4.2, in the following form

$$\delta\mathbf{b}_2(\mathbf{X}) = \frac{0.3(\hat{\mathbf{y}} \sin \theta - \hat{\mathbf{x}} \cos \theta) \sin(x \cos \theta + y \sin \theta)}{e^{[(x/25-1)^2+(y/25-1)^2]^4}} \quad (4.15)$$

The image of the magnitude of the synthesized field is shown in the bottom left panel in Fig 4.2. The fieldlines of the mean field \mathbf{B}_0 , the mean field with the global component $\mathbf{B}_0 + \delta\mathbf{b}_1$, and the mean field with both the global and local components $\mathbf{B}_0 + \delta\mathbf{b}_1 + \delta\mathbf{b}_2$, are shown in the bottom right panel as the green, blue and red lines respectively. Notice the small scale wavy structure

in the red lines in the bottom right panel with respect to the variations in the region that has the local component in the bottom left panel.

We summarize the two-scale synthesis as the follow algorithm

Algorithm 1 The two-scale synthesis

1. Divide the whole domain into cubes with the edge size $L = 1/K_2$
 2. Specify the background mean field \mathbf{B}_0
 3. Synthesize the global components $\delta\mathbf{b}_1$ with the wave number in $[K_1, K_2)$
 4. Calculate the local average in each cube
 5. Synthesize the local components $\delta\mathbf{b}_2$ with the wave number in $[K_2, K_3)$
 6. Align the local components in each cube with the local average
-

4.3 Synthesis of the Two Scale Anisotropy

Here we outline the two-scale synthesis in detail. We first specify S_0 , S_1 and S_2 in Figure 4.1. And then we divide the whole region into blocks of size L_2 determined by S_1 . Next, the large scale synthesis is described as

$$\mathbf{B}_1 = B_0 \hat{\mathbf{z}} + \delta\mathbf{b}_1(x, y, z) \quad (4.16)$$

$$\delta\mathbf{b}_1(x, y, z) = \sum_{n=1}^{N_m} A(k_n) \hat{\xi}_n \exp(2\pi i k_n z'_n + i\beta_n) \quad (4.17)$$

$$\hat{\xi}_n = \cos \alpha_n \hat{\mathbf{x}}'_n + i \sin \alpha_n \hat{\mathbf{y}}'_n \quad (4.18)$$

$$\begin{Bmatrix} \mathbf{x}' \\ \mathbf{y}' \\ \mathbf{z}' \end{Bmatrix} = \mathbf{RM}(\theta_n, \phi_n) \begin{Bmatrix} \mathbf{x} \\ \mathbf{y} \\ \mathbf{z} \end{Bmatrix} \quad (4.19)$$

$$\mathbf{RM}(\theta, \phi) = \begin{pmatrix} \cos \theta \cos \phi & \cos \theta \sin \phi & -\sin \theta \\ -\sin \phi & \cos \phi & 0 \\ \sin \theta \cos \phi & \sin \theta \sin \phi & \cos \theta \end{pmatrix} \quad (4.20)$$

$$A^2(\mathbf{k}_n) = \frac{P(k_n, \theta_n) \Delta k^3}{\sum P(k_n, \theta_n) \Delta k^3} \quad (4.21)$$

$$P(k_n, \theta_n) = \frac{\sigma_B^2 L^3 \exp\{-(k_n L)^{1/3} \sin \theta_n / |\cos \theta_n|^{2/3}\}}{6\pi (k_n L |\cos \theta_n|)^{5/3} (1 + k_n L |\cos \theta_n|)^{5/3}} \quad (4.22)$$

Where $A(k_n)$ is the amplitude of the wave mode k_n for wave mode n , α_n represents polarization, β_n phase, θ_n and ϕ_n the direction of propagation with z_0 as the polar axis. Note that the above operations are performed at large scale, and the turbulent magnetic field so generated is a uniform field plus a globally quasi-isotropic random part because the anisotropy is moderate at large scales.

Simulation Results									
Case	Energy	r_g	σ^2	L_c	λ_{min}/r_g	λ_{max}/r_g	κ_{\perp}	κ_{\parallel}	$\kappa_{\perp}/\kappa_{\parallel}$
-	MeV	10^{-3} AU	AU	10^{-2} AU	1	1	$10^{18} \frac{cm^2}{s}$	$10^{19} \frac{cm^2}{s}$	0.1
1	1.0	0.193	1.0	1.0	0.519	5190	3.01	1.64	1.83
2	3.16	0.343	1.0	1.0	0.2917	2917	7.42	3.54	2.09
3	10.0	0.611	1.0	1.0	0.1637	1637	18	10.2	1.8
4	31.6	1.09	1.0	1.0	0.0915	915.4	48	31.1	1.55
5	100	1.98	1.0	1.0	0.0506	505.8	137	94.8	1.45
6	316	3.70	1.0	1.0	0.0270	270.0	342	241	1.35
7	1000	7.59	1.0	1.0	0.0133	132.6	682	596	1.15
8	10000	48.6	1.0	1.0	0.0021	20.58	2135	3176	0.67

Table 4.1: **The results are from the correspondent cases using the two-scale Goldreich Sridhar type turbulent magnetic field algorithm.**

Next, we calculate the local components with wavenumber as in $[S_1, S_0)$ in Figure 4.1. We need to determine the local magnetic field components within each block of the size L_2 . We first calculate the average field in each

block. For the j^{th} block we have

$$\mathbf{b}_{0,j} = \int_{j^{th} \text{ block}} \mathbf{B}_1(\mathbf{X}) d\mathbf{X} \quad (4.23)$$

Therefore we know the local average of the magnetic field. Now suppose a vector point (x, y, z) is in the j^{th} block whose center is (x_j, y_j, z_j) . Then we calculate the corresponding η_j and ν_j in that block to rotate the z axis to align with the local average magnetic fieldline, which are used to rotate the point (x, y, z) to the coordinate system that align with the local magnetic fieldline

$$\begin{pmatrix} \mathbf{x}' \\ \mathbf{y}' \\ \mathbf{z}' \end{pmatrix} = \mathbf{RM}(\eta_j, \nu_j) \begin{pmatrix} \mathbf{x} - \mathbf{x}_j \\ \mathbf{y} - \mathbf{y}_j \\ \mathbf{z} - \mathbf{z}_j \end{pmatrix} \quad (4.24)$$

Next we calculate the local components by

$$\delta \mathbf{b}_2(x, y, z) = \sum_{n=m+1}^{N_n} A(k_n) \hat{\xi}_n \exp\{2\pi i k_n z'' + i\beta_n\} h(\mathbf{x}'', k_n) \quad (4.25)$$

$$A^2(\mathbf{k}_n) = \frac{P(k_n, \theta_n) \Delta k^3}{\sum P(k_n, \theta_n) \Delta k^3} \quad (4.26)$$

$$P(k_n, \theta_n) = \frac{\sigma_B^2 L^3 \exp\{-(k_n L)^{1/3} \sin \theta_n / |\cos \theta_n|^{2/3}\}}{6\pi (k_n L |\cos \theta_n|)^{5/3} (1 + k_n L |\cos \theta_n|)^{5/3}} \quad (4.27)$$

$$h(\mathbf{x}'', k_m) = \frac{C}{e^{[2k_m \sqrt{x''^2 + y''^2 + z''^2}]^{100}}} \quad (4.28)$$

$$\hat{\xi}_n = \hat{\phi}(x'', y'') \quad (4.29)$$

$$\begin{pmatrix} \mathbf{x}'' \\ \mathbf{y}'' \\ \mathbf{z}'' \end{pmatrix} = \mathbf{RM}(\theta_n, \phi_n) \begin{pmatrix} \mathbf{x}' \\ \mathbf{y}' \\ \mathbf{z}' \end{pmatrix} \quad (4.30)$$

The θ_n and ϕ_n are randomly selected as in the global case. And the amplitude of each mode is determined by the GS type spectrum function while each $\hat{\xi}_n$ is chosen to conserve the zero divergence condition for each component. Note that $h(\mathbf{x}'', k)$ function is used to preserve the continuity between the interface of the neighboring blocks. Take the local mode shown in the upper right panel in Fig 4.2 for example, in the local x'', y'', z'' coordinate system it is described generally as

$$\delta \mathbf{b}_2 = A(k_n) \frac{x'' \hat{\mathbf{e}}_{y''} - y'' \hat{\mathbf{e}}_{x''}}{\sqrt{x''^2 + y''^2}} \frac{C e^{ik_n z'' + i\beta_n}}{e^{[2k_n \sqrt{x''^2 + y''^2 + z''^2}]^{100}}} \quad (4.31)$$

One could verify that

$$\nabla \cdot \delta \mathbf{b}_2 = \frac{\partial \delta b_{2,x''}}{\partial x''} + \frac{\partial \delta b_{2,y''}}{\partial y''} = 0 \quad (4.32)$$

This zero divergence is conserved under the rotation $\mathbf{RM}(\theta_n, \phi_n)$ from the coordinate (x'', y'', z'') to (x', y', z') , and then the rotation $\mathbf{RM}(\eta_j, \nu_j)$ to the coordinate $(x - x_j, y - y_j, z - z_j)$.

Getting back to the synthesis, we put the above components together as the last step to have

$$\mathbf{B}(\mathbf{X}) = \mathbf{B}_0(\mathbf{X}) + \delta \mathbf{b}_1(\mathbf{X}) + \delta \mathbf{b}_2(\mathbf{X}) \quad (4.33)$$

The full zero divergence check of the small scale local components $\delta \mathbf{b}_2(\mathbf{X})$ is given in the Appendix.

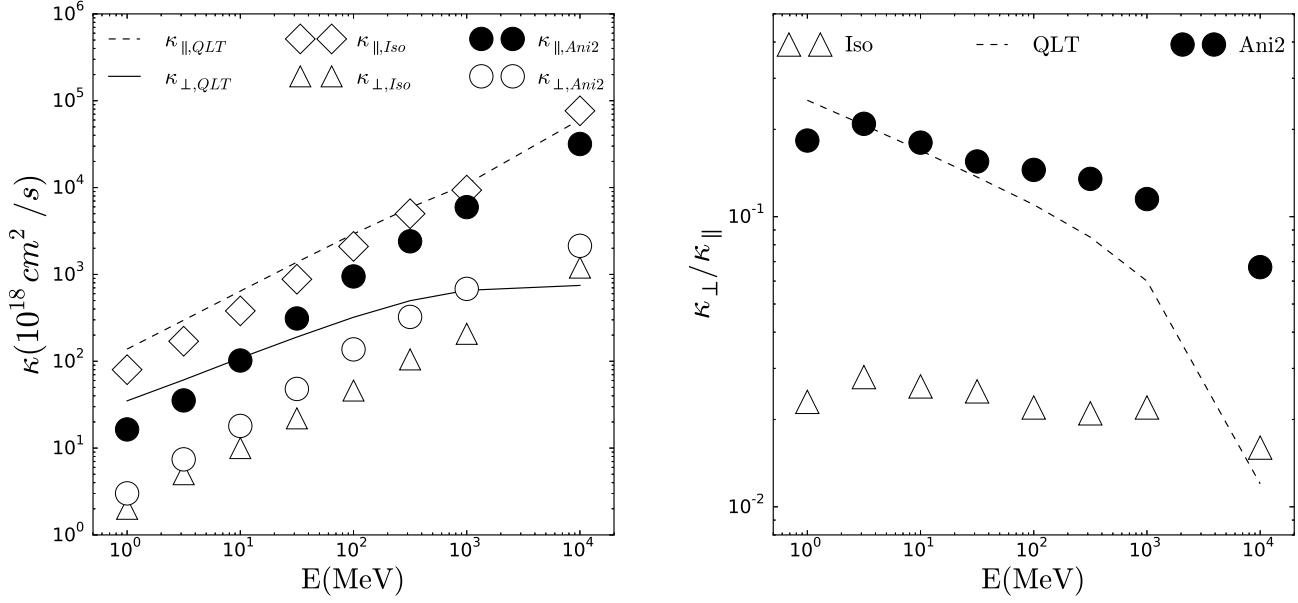


Figure 4.3: The transport coefficients calculated by the numerical experiments in Table 4.1. The left panel shows perpendicular and parallel transport coefficients in three turbulent magnetic field models, i.e. isotropy, global anisotropy and the local anisotropy, as a function of the particle's energy. The white and black circles, κ_{\perp} and $\kappa_{||}$ respectively, are values in Table 4.1. The diamonds and triangles are simulation results from cases with the isotropic turbulence power spectrum as in Giacalone & Jokipii (1999). The diamond is the parallel diffusion coefficient while the triangle the perpendicular coefficient. The dashed line and solid line are the coefficients calculated by equations (4.34) and (4.35) respectively. The right panel shows their ratio as the function of proton energy. The black circles are $\kappa_{\perp}/\kappa_{||}$'s from Table 4.1, the triangles represent simulation results with isotropic turbulence model, and the dashed line is from equations (4.34) and (4.35) using GS type power spectrum.

4.4 Transport Experiments and Results

We used 400 modes covering the wavenumber range from $2\pi/100L_c$ to $2\pi/.01L_c$ to synthesize the two-scale anisotropic turbulent magnetic fields.

We used the same simulation experiment to calculate the parallel and perpendicular transport coefficients as described in Chapter 3. The cases and results

are summarized in Table 4.1 and Figure 4.3. From Chapter 3 we learned from our numerical experiment that the global model has similar effects on the transport coefficients as the isotropic model. Therefore we only compare the results from the multi-scale synthesis with those isotropic cases as in Chapter 3 and Giacalone & Jokipii (1999). We also take the estimate of the perpendicular and parallel transport coefficients by the Quasi-Linear Theory (Jokipii, 1966) in Chapter 3 for comparison:

$$\kappa_{\perp} \cong \frac{vL_c \sigma_B^2}{6 B_0^2} \quad (4.34)$$

$$\kappa_{\parallel} = \frac{3v^3 B_0^2}{\pi \Omega_0^2 L_c \sigma_B^2} \int_0^1 \mu(1 - \mu^2) \left(1 + \frac{\Omega_0 L_c}{v\mu}\right)^{5/3} d\mu \quad (4.35)$$

Here μ is the cosine of the pitch angle, L_c is the correlation length of the magnetic turbulence, v is the speed of the charged particle, Ω_0 is the gyro frequency in the background magnetic field B_0 , and σ_B^2 is the variance of the turbulent magnetic field. These estimates are shown as the dashed or solid lines in Figure 4.3 for comparison. Notice that these estimates are not made from theories that are proposed for the two scale, localized anisotropic turbulent magnetic field model, therefore they are different from the numerical simulation results for the isotropic and the locally anisotropic cases. However, they suggest a proper orders of magnitude for the transport coefficients.

From the left panel in Figure 4.3 we find that in the two-scale anisotropic model the perpendicular transport is enhanced while the parallel transport is inhibited compared with the isotropic magnetic turbulence model. This is probably because of the local anisotropy of the magnetic field incorporated in

the new algorithm presented in this chapter, given the results and conclusion of Chapter 3 that the global anisotropy has similar effects on the charged particle transport as the isotropic model. However, the quantitative effect could only be determined specifically by a theoretical transport model based on a turbulent magnetic field model that explicitly holds the local anisotropy feature such as proposed here in the multi-scale model.

We also find from the left panel in Figure 4.3 that the difference between the isotropic and the two-scale anisotropic cases are more significant for the charged particles with lower energies. This is probably due to the fact that in the GS type MHD turbulence the anisotropy is increased at shorter wave lengths l 's, which are closer to the resonance scales of the lower energy charged particles. (Consider the resonance scale l_{res} for a charged particle scattering in the turbulent magnetic field. It is given by $k_{res} = 2\pi/l_{res} = \Omega_0/v_{\parallel}$. Therefore $l_{res} \sim R_g$, which is about the gyro radius of the charged particle.) And the enhanced anisotropy significantly changes the small scale field structure and geometry, therefore has larger effects on the lower energy particle transport.

From the right panel in Figure 4.3 we could observe that the ratio of perpendicular to parallel transport coefficients, $\kappa_{\perp}/\kappa_{\parallel}$, is about one order of magnitude larger in the model with the local anisotropy than that with the isotropy. This ratio is an important quantity in charged particle shock acceleration. This implies higher acceleration efficiency in this type of turbulent

magnetic fields.

4.5 Conclusion

In this chapter, we propose a systematic, multi-scale, parameterized method to generate the zero-divergence, continuous, anisotropic and scale-dependent localized turbulent magnetic field. We adapt the two-scale algorithm, and use the wave modes with finite support in real space to align the small scale local components with the local average fieldlines. We performed test particle numerical experiment to calculate transport coefficients and found that: 1) parallel transport decreases and perpendicular transport increases compared with the isotropic and globally anisotropic models, 2) the difference is enhanced where the local anisotropy is enhanced, and 3) the ratio $\kappa_{\perp}/\kappa_{\parallel}$ is an order of magnitude higher in this local anisotropy synthesis than those in the isotropic and globally anisotropic models. The next step is to develop a transport theory that could explicitly describe the effect of the local anisotropy. Another interesting problem is to investigate the charged particle shock acceleration given the turbulent magnetic field with local anisotropy around the shocks. Our future work will try to answer these questions.

Chapter 5

Applications to Solar Wind data

The multi-scale method proposed in last chapter (Chapter 4) can be used to synthesize any non-isotropic turbulent magnetic field, as long as the power spectrum is known as a function of scales. In this chapter, we propose a simple power spectrum synthesis method based on Fourier analysis to extract the large and small scale power spectrum from any single spacecraft observation with a long enough period and a high sampling frequency. We apply the method to the solar wind measurement by the magnetometer onboard the ACE spacecraft and regenerate the large scale isotropic 2D spectrum and the small scale anisotropic 2D spectrum.

5.1 Introduction

In the last chapter (hereafter referred as Chapter 4) we proposed a multi-scale synthesis method for the anisotropic turbulent magnetic fields. This synthesis method could be generalized as

$$\mathbf{B}(\mathbf{X}) = \underbrace{\mathbf{B}_0(\mathbf{X})}_{k < K_1} + \underbrace{\delta\mathbf{b}_1(\mathbf{X})}_{k \in [K_1, K_2]} + \underbrace{\delta\mathbf{b}_2(\mathbf{X})}_{k \in [K_2, K_3]} + \dots \quad (5.1)$$

Where B_0 is the global average of the magnetic field, $\delta\mathbf{b}_1$ is the large scale turbulent field component following the large scale power spectrum and, $\delta\mathbf{b}_2$ is the small scale turbulent field component following the small scale power spectrum. And both the large and small scale power spectrum follows the Goldreich & Sridhar (1995). We run test particle simulations in the two-scale synthesis and found that the parallel transport is decreased and the perpendicular transport is increased for charged particles with energy from 1 MeV up to 10GeV.

In practice, it is sometimes difficult to determine the proper type of turbulent magnetic field model given limited single spacecraft observations. However, our two scale synthesis method in Chapter 4 could also be applied to the general non-isotropic turbulent magnetic field models, given the large and small scale power spectrum. The charged particle transport could be calculated and compared in this way.

Recently, Horbury et al. (2008) applied the wavelet method for measuring the power spectra index along and normal to the local average of the magnetic field. In this chapter, we will move one step forward by proposing a method

to generate two dimensional power spectrum based on the time series data from a single spacecraft based on the similar idea. The general method is introduced in section 2, we apply our method on the data set from ACE about the solar wind in section 3. Section 4 is our conclusion.

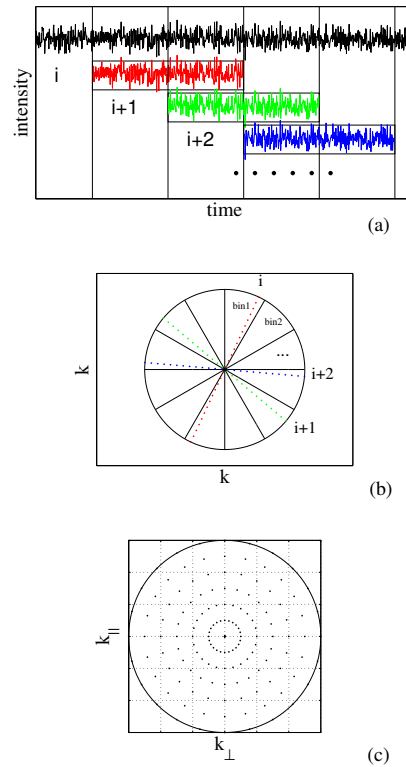


Figure 5.1: A schematic plot of the anisotropic power spectrum extraction from the time series data set. A sliding window is used for the statistically better result shown in the top and middle panel. As an example, the i^{th} , $i + 1^{th}$ and $i + 2^{th}$ slice of data are selected as in red, green and blue from the whole time series in the top panel. In the middle panel, the i^{th} , $i + 1^{th}$ and $i + 2^{th}$ are put into the corresponding bins according to their orientation relative to the local mean field. The bottom panel is the result of interpolation around the one dimensional power spectra in all the recorded directions.

5.2 Data process techniques and assumptions

For a spacecraft such as ACE, the magnetometer onboard would detect a time series data of the magnetic field in a given coordinate system (e.g. Geocentric solar ecliptic, abbreviated as GSE) with a certain data sampling rate. Although the field data has three channels on the three axes, this time series data is one dimensional in space since the path of the spacecraft in the reference frame of the moving solar wind is a line for a moderate time span.

The first assumption is the Taylor's hypothesis, which relates the time series to the corresponding line of points in the space. This is described as

$$P_{ij}(g) = \frac{1}{V_w} \int dx R_{ij}(x, 0, 0, 0) e^{i2\pi f x / V_w} \quad (5.2)$$

Where $P(g)$ is the observed frequency power spectrum, V_w is the solar wind flow speed, and

$$R_{ij}(x, 0, 0, 0) = \langle B_i(x' + x, y', z', t') B_j(x', y', z', t') \rangle \quad (5.3)$$

is the two point correlation function along the x axis, which is the direction of the solar wind in the GSE coordinate. Take consideration a certain period of time, eg 256 seconds, although the solar wind flow is along the x direction, the average magnetic field could be in arbitrary direction. Denote angle between them as θ_B . From the above equations we know that the $P(g)$ is actually the power spectrum in a line with angle θ_B to the average field. We assume

the solar wind magnetic turbulence is axisymmetric. Consequently if we can measure the power spectra that can cover all the θ_B , we could patch them together to get the power spectrum in the whole wave number space of $(k_{\perp}, k_{\parallel})$ (the power spectrum synthesis is described in detail in the appendix). Therefore, that the spacecraft observations will cover all the orientations under the ergodic hypothesis of turbulence, is our final assumption.

We use the ACE spacecraft 1-second-period data set of the magnetic field to reconstruct the power spectra for the small scale power spectrum, and the 4-minute-period data set for the large scale power spectrum. The 1-second data spans from the 68th day to the 216th day in 2009, while the 4-minute data spans from the 68th day in 2009 to 67th day in 2010. We use the average solar wind speed, 400 km/s, for both cases in this chapter. The process is illustrated as in Figure 5.1. In the upper panel, the black line represents a high frequency time series data over a long period. We then take a lot of short period slices (256 sample points slices for the 1-second data and 64 sample points slices for the 4-minute data), with a short sliding window for better statistics. As in the middle panel, we divided the angle of θ_B into a lot of bins. We calculate each θ_B for each slice of magnetic field data, and then put the slice into the corresponding bin by the angle. In this way we get the two dimensional power spectrum represented by the blue points in the bottom panel. We then can use interpolation to calculate the power spectrum at any given point of $(k_{\perp}, k_{\parallel})$ in the bottom panel.

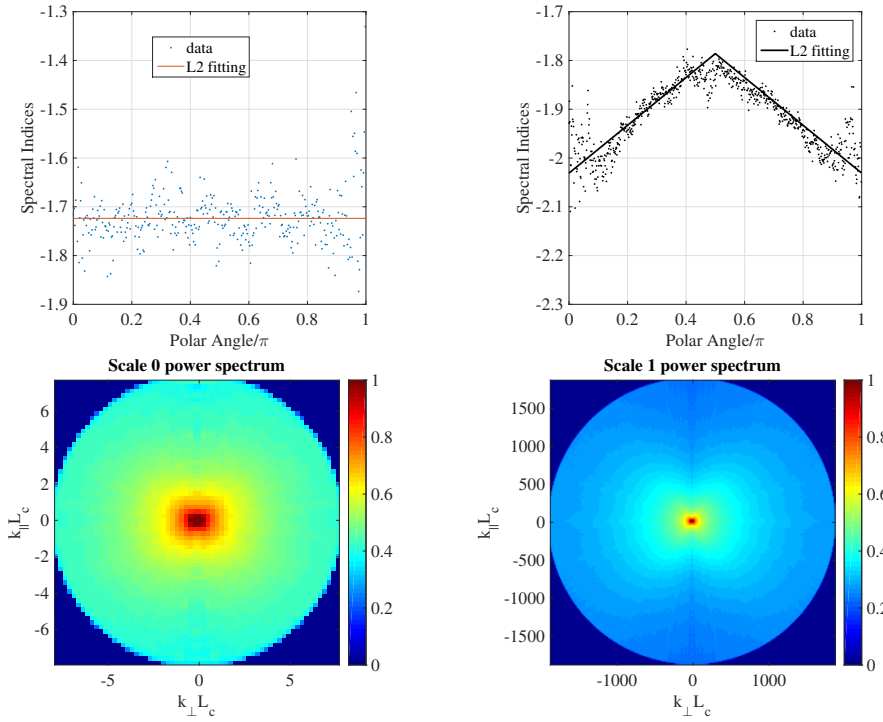


Figure 5.2: **The power spectra indices and the 2D power spectra. The upper left panel shows the large scale power spectra indices as a function of the polar angles. The upper right panel shows the corresponding indices in the small scales. The bottom left panel shows the large scale power spectrum and the bottom right one the small scale power spectrum.**

5.3 Power Spectrum Synthesis

For a two dimensional function such as $g(k_{\perp}, k_{\parallel})$, we can write the 2D Fourier transform as

$$F(k_{\perp}, k_{\parallel}) = \int \int dx dy g(x, y) \exp\{-i(k_{\perp}x + k_{\parallel}y)\} \quad (5.4)$$

where in our case the $g(x, y)$ is the two dimensional "observation" of magnetic field data associated with the above power spectrum. Here x and y are the coordinates normal to each other. Suppose we know many slices of $F(k_{\perp}, k_{\parallel})$ through the origin, which means if we choose many x'_i and y'_i , equivalent to

rotating of x and y by an angle of θ_i and we know the $F(k_{\perp,i}, k_{\parallel,i})$ along each of the new x'_i , then we can reconstruct the original $D(k_{\perp}, k_{\parallel})$.

Since we just need to know the $P(k_{\perp,i}, k_{\parallel,i})$ along x'_i , which is

$$F(k_{\perp,i}, 0) = \int \int dx'_i dy'_i \left| \frac{\partial(x'_i, y'_i)}{\partial(x, y)} \right| g(x'_i, y'_i) \exp\{-i(k_{\perp} x'_i)\} \quad (5.5)$$

$$= \int dx'_i \exp\{-ik_{\perp,i} x'_i\} \left[\int g(x'_i, y'_i) dy'_i \right] \quad (5.6)$$

$$= \int dx'_i \exp\{-ik_{\perp,i} x'_i\} g(x'_i) \quad (5.7)$$

where $\left| \frac{\partial(x'_i, y'_i)}{\partial(x, y)} \right|$ is the Jacobian between coordinate transformation,

$$g(x'_i) = \int g(x'_i, y'_i) dy'_i \quad (5.8)$$

if we can estimate $g(x'_i)$ from a set of single-path observations like ACE, we can reconstruct the two-dimensional power spectrum. If we name $g(x, y)$ as the distribution of the random variable B_x from the time series of observations, $g(x)$ is the marginal distribution. For the ACE satellite data, we need to estimate the marginal distribution based on a single satellite observation through a line in two-dimensional space assuming axis symmetry to the local mean field.

We assume that the random variables above and under the path $y'_i = 0$ will cancel each other, and then

$$\hat{g}_1(x'_i) = \int g(x'_i, y'_i) dy'_i = \sum_k g(x'_i, y'_{i,k}) \Delta(k) = g(x'_i, 0) \quad (5.9)$$

or we assume that the marginal function $g(x)$ and $g(y)$ are independent and hence

$$\hat{g}_2(x'_i) = \int g(x'_i, y'_i) dy'_i = \int g(x'_i)g(y'_i) dy'_i = g(x'_i) \int g(y'_i) dy'_i = Cg(x'_i) \quad (5.10)$$

where C is a normalization factor. We can use either $\hat{g}_1(x'_i) = g(x'_i, 0)$ or $\hat{g}_2(x'_i) = g(x'_i)$ (upon normalization) as the estimator function of the marginal distribution function. Then by Fourier transforming each path of $y'_i = 0$ in (x'_i, y'_i) with respect to (x, y) , we can calculate many slices of the original $F(k_\perp, k_\parallel)$, and we can now reconstruct it by interpolation within each slice. Once we know the $F(k_\perp, k_\parallel)$, we can calculate two-dimensional power spectrum which tells us the distribution of each wave mode in the two-dimensional wave number space.

5.4 Results

The results are shown in the Figure 5.2. The two upper panels show the power spectra indices as a function of the polar angle and their least square fittings. The large scale power spectra index is fitted to be the line $y=-1.72$ as shown in the upper left panel in the Figure 5.2, while the small scale power spectrum shows significant anisotropy that changes with the polar angle. The power spectra index is about -2 in the parallel direction with respect to the local average field and is about -1.8 along the perpendicular direction. The two bottom panels show the 2D power spectra. The large scale power spectrum

resembles the isotropic turbulence while the small scale one shows significant anisotropy in different directions.

5.5 Conclusion

In this chapter, we propose a general method to generate the two scale power spectra for the multi-scale anisotropic turbulence magnetic field synthesis. The large scale power spectra is isotropic with the power spectra index -1.7 . The small scale power spectra is anisotropic. The power spectra index changes from -1.8 in the perpendicular direction to the local average field to -2 in the parallel directions. This offers a possible way to calculate charged particle transport in the turbulent magnetic field given a long enough single spacecraft observations of the magnetic field and plasma flow velocity.

Chapter 6

Summary

In this dissertation we investigate the charged particle pitch angle scattering in the solar wind type turbulent magnetic field. This is the first high precision pitch angle scattering calculation in the solar wind type turbulence magnetic field with a nearly constant magnitude. We also introduce a new method to accurately determine the pitch-angle diffusion coefficients. A future work would be apply this optimization in the three dimensional isotropic turbulent magnetic field models while performing both the numerical experiment on the scattering and the ones on the diffusion for charged particles to observe the effects of the optimizations.

We introduce the problem that different MHD turbulence model could have different effects on charged particle transport. We also explained that there are three methods to approach this problem: pure theoretical analysis, direct MHD turbulence simulation coupled with particle tracking codes, and finally the synthesis of different turbulent magnetic field models plus test

particle simulations and highlighted the last method. We also outlined that a successful synthesis needs to satisfy at least the following requirements: a) the field has to have zero divergence, b) the field has to be continuous, c) the field has to have the anisotropic spectrum, and d) the field has better to explicitly have the scale dependent anisotropy.

We demonstrate that it is difficult to satisfy all the conditions at once in the same synthesis. Instead, as the first step, we synthesized the globally anisotropic fields with all conditions except for d), and carried out test particle simulations to calculate the transport coefficients in the global anisotropy and compared with the isotropic models. We found that there is no significant difference between the global anisotropy and isotropy of the MHD turbulence on particle transport.

We then provide the synthesis framework for anisotropic magnetic turbulence that satisfies all the conditions a) through d). The framework provides for the first time a multi-scale synthesis of the scale-dependent, anisotropic turbulent magnetic field. The success construction of the magnetic field with anisotropy also provides a proof for the existence of the GS-type anisotropic turbulence. We also adapt the two-scale algorithm to construct a fluctuating magnetic field and performed test particle numerical experiment to calculate transport coefficients. We find that: 1) parallel transport decreases and perpendicular transport increases compared with the isotropic and globally anisotropic models, 2) the difference is enhanced where the local anisotropy

is enhanced, and 3) the ratio $\kappa_{\perp}/\kappa_{\parallel}$ is an order of magnitude higher in this local anisotropy synthesis than those in the isotropic and globally anisotropic models. The next step is to develop a transport theory that could explicitly describe the effect of the local anisotropy. Another interesting problem is that this new transport features may modify the current cosmic rays modulation in the heliosphere by the turbulent solar wind magnetic field. We would like to answer the questions such as: if we use the GS type turbulence to simulate the fluctuating magnetic field in the heliosphere, how would that affect the observed cosmic rays modulations quantitatively during the solar cycles? Further more, if we use the anisotropic turbulence model to simulate the fluctuating magnetic field in the interstellar medium, how would this change the distribution of the sources given the observation of the galactic cosmic rays? Yet another related problem is to investigate the charged particle shock acceleration given the turbulent magnetic field with local anisotropy around the shocks. This different transport features from the previous magnetic turbulence model would change the efficiency of the shock acceleration and hence modify the estimate of the largest energy a charged particle could reach from the acceleration site such as solar flare and supernovae.

And finally in the last chapter, we propose a general method to generate the two scale power spectra for the multi-scale anisotropic turbulence magnetic field synthesis. This is a method to reconstruct the magnetic field spectrum from the real time spacecraft dataset. This offers a possible way to calculate

charged particle transport in the turbulent magnetic field given a long enough single spacecraft observations of the magnetic field and plasma flow velocity for any satellite. By applying this method to the solar wind magnetic field data, we reconstruct the non-isotropic magnetic field power spectrum, and we also find that the large scale power spectra is isotropic with the power spectral index -1.7 . The small scale power spectra is anisotropic. The power spectra index changes from -1.8 in the perpendicular direction to the local average field to -2 in the parallel directions. This data-driven power spectrum could then be fed into our framework of the field synthesis and generate a more precise particle transport calculation that could lead to better descriptions of the energetic particle motions in the Heliosphere, which are important for the estimations of shock accelerations related to flare and coronal mass ejections, space weather forecasting, and in situ radiation environment evaluations in space, etc.

Appendix A

Numerical Integrators

Numerical integrators are used in Chapter 2-4 to track (push) the charged particle's trajectory in different turbulence models. Usually a 5th order adaptive Runge-Kutta method is accurate enough to integrate a particle's trajectory over several thousand gyro-periods. This is true when estimating the spatial transport coefficients. Therefore, we could choose the 5th order adaptive Runge-Kutta method or the Bulirsch-Stoer method to push particles as in Chapter 3 and 4. However, when calculating the pitch-angle diffusion coefficient as in Chapter 2, we need to use higher order numerical algorithms. This is because the scattering happens very fast and the pitch-angle diffusion coefficient is a function that varies over different pitch angles. This is the reason that we chose the 8th order adaptive Runge-Kutta method. In this Appendix we will test the performance of the numerical integrator, the 8th order adaptive Runge-Kutta method. And we will also compare it with the 5th order adaptive Runge-Kutta method as well as the Bulirsch-Stoer method. A simple

test is the two-body problem that says a point mass M1 and a point mass M2 are both rotating around their mass center. We have assumed that the mass center does not move in this simplified case. Since the motion of the two point masses is in the same plane, we could just use a two dimensional Cartesian coordinate system. Let the mass center resides in the origin. Suppose M1 and M2 are both on the x axis initially. So their positions are $(x_{10}, 0)$ and $(x_{20}, 0)$. For M1, its initial velocity is $(0, v_{10})$, while for M2, $(0, v_{20})$. Here v_{10} and v_{20} are in the opposite directions for simplicity. In this case, the set of differential equations for the two point masses could be rewritten as

$$\mathbf{y}' = \mathbf{A} \cdot \mathbf{y} \quad (\text{A.1})$$

$$\mathbf{y}(\mathbf{0}) = \mathbf{y}_0 \quad (\text{A.2})$$

Here $\mathbf{y} = (\mathbf{x}_1(\mathbf{t}), \mathbf{y}_1(\mathbf{t}), \mathbf{u}_1(\mathbf{t}), \mathbf{v}_1(\mathbf{t}), \mathbf{x}_2(\mathbf{t}), \mathbf{y}_2(\mathbf{t}), \mathbf{u}_2(\mathbf{t}), \mathbf{v}_2(\mathbf{t}))$ represents the positions and velocities of point mass 1 and 2 in the x-y coordinate at time t. Since the matrix \mathbf{A} is constant over time, this is a linear system. Also this system's total energy is conserved, which is just the sum of their kinetic energies and the gravitational potential energy. However, for both Runge-Kutta method and Bulirsch-Stoer method, the total energy is changing with the integration time due to the numerical errors. The numerical effects are shown in Figure A.1. It takes 10^6 periods for the 8th order adaptive Runge-Kutta method to have less than 0.4% error, while the Bulirsch-Stoer method takes about 2×10^5 periods and the 5th order Runge-Kutta method takes about 10^5 periods.

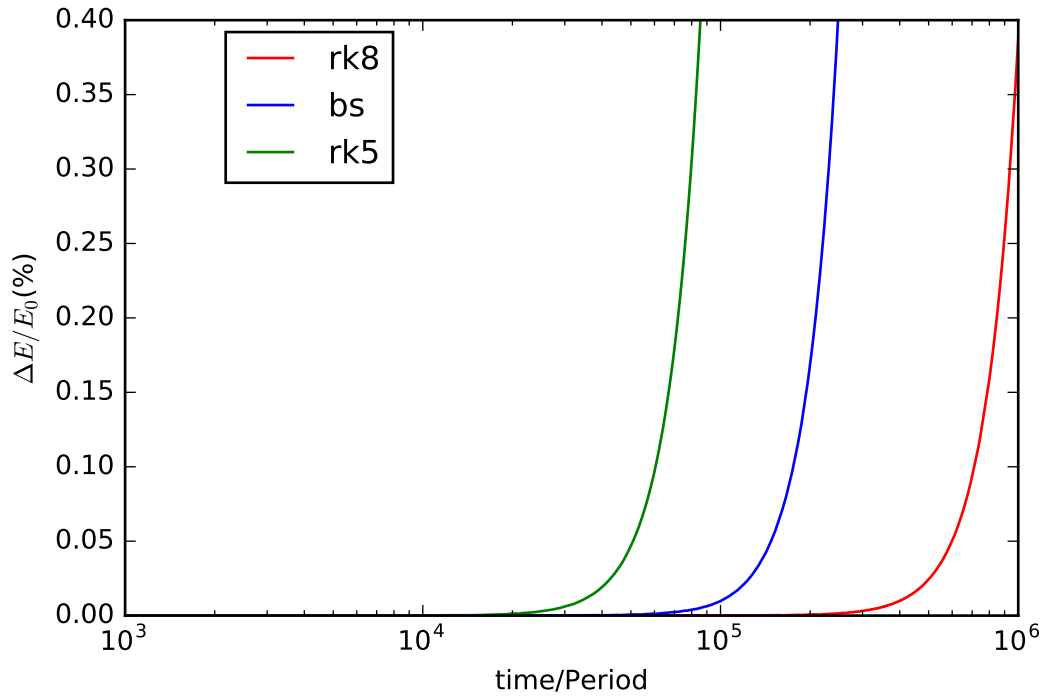


Figure A.1: The simplified Two Body problem is used to test the numerical effects of the 8th order and 5th order adaptive Runge-Kutta method, as well as the Bulirsch-Stoer method.

The next test is the restricted three body problem, which is a nonlinear problem. As a simplified case, we add another massless test point mass m in the same plane as the above two body system. This is a so called restricted coplanar three body problem. Since the two body problem has a closed form analytical solution, we only need to solve the test point mass m 's motion. The nonlinearity lies in the fact that if we rewrite its equation as the format of A1 and A2, the matrix A will no longer be constant but changes with time and position relative to the center of mass. However, the total energy of the test point mass m is still constant in this case. But due to the nonlinearity, the

numerical effect will be chaotic in this case. This means that if we integrate the equations of its motion over time, there will be some moment after which the particles' motion is non-realistic because the growth of the error is out of control. Shown in Figure A.2 is the evolution of the test particle's total energy over time. One would observe the lowest accuracy algorithm, the 5th order adaptive Runge-Kutta method, first arrives at the state of chaos as the green line at about less than 100 time steps (about 15 periods). And a better algorithm is the Bulirsch-Stoer method, which fails at about 400 time steps (about 65 periods). The best one is the 8th order adaptive Runge-Kutta method, which lasts until about 600 time steps (about 100 periods).

In Chapter 2-4 in this dissertation, we used the 8th order adaptive Runge-Kutta method for the pitch angle diffusion coefficient calculation, which is believed to require a high order accuracy numerical algorithm. We used the 5th order adaptive Runge-Kutta method for the spatial diffusion coefficient calculation, and we believe it is accurate enough and could be replaced by the Bulirsch-Stoer method.

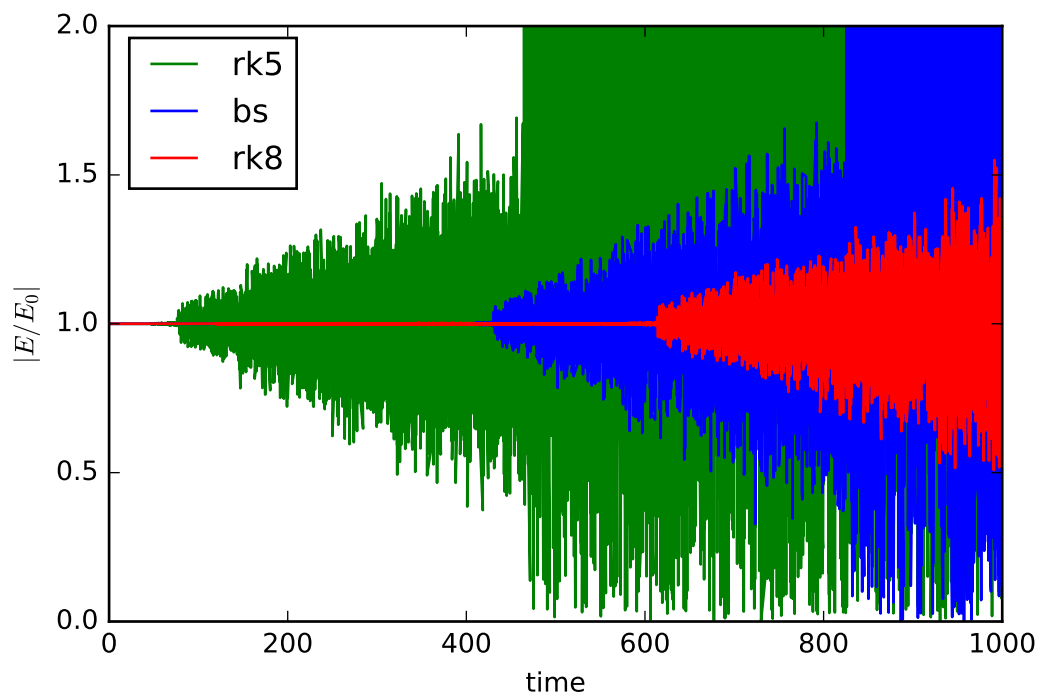


Figure A.2: The simplified Restricted Three Body problem is used to test the numerical effects of the 8th order and 5th order adaptive Runge-Kutta method, as well as the Bulirsch-Stoer method.

Bibliography

- Armstrong J. W., Rickett B. J., & Spangler S. R., 1995, *ApJ*, 443, 209
- Beatty J. J. and Westerhoff S., 2009, *Annu. Rev. Nucl. Part. Sci.*, 59:319
- Belcher J. W. and Davis L., Jr., 1971, *J. Geophys. Res.* 76, 3534
- Beresnyak, A., Yan H., & Lazarian A., 2011, *ApJ*, 728, 60
- Bieber, J. W., Wanner, W., & Matthaeus, W. H. 1996, *J. Geophys. Res.*, 101,
2511
- Boldyrev S. 2006, *Phys. Rev. L*, 96, 115002
- Chandran, B. D. G., 2000, *Phys. Rev. L*, 85, 4656
- Cho, J., Lazarian, A., & Vishniac, E. T. 2002, *ApJ*, 564, 291
- Dasso S., Milano L. J., Matthaeus W. H., and Smith C. W., 2005, *ApJ*. 635,
L181
- Dobrowolny, M., Mangeney, A., & Veltri, P., 1980, *Phys. Rev. L*, 45, 144
- Earl, J. A. 1974, *ApJ*, 193, 231

- Florinski, V., et al. 2010, *ApJ*, 719, 1097-1103
- Funsten, H. O., et al. 2009, *Science*, 326, 964
- Fuselier, S. A., et al. 2009, *Science*, 326, 962
- Giacalone, J., & Jokipii, J. R., 1999, *ApJ*, 520, 204
- Goldreich, P. & Sridhar, H., 1995, *ApJ*, 438, 763
- Gray, C., Pontius, D. H., Jr., & Matthaeus, W. H. 1996, *Geophys. Res. Lett.*, 23, 965
- Hairer, E., Nørsett, S. P., and Wanner, & G. 1993, *Solving Ordinary Differential Equations I. Nonstiff Problems*, 2nd ed, New York: Springer
- Heerikhuisen, J., et al. 2010, *ApJ*, 708, L126
- Horbury, T. S., Forman M., & Oughton S. 2008, *Phys. Rev. L*, 101, 175005
- Hess, V. F., 1912, *Physikalische Zeitschrift* 13: 1084
- Hussein, M., Tautz, R. C., Shalchi, A., *J. Geophys. Res.*, 120, 6, 4095
- Jokipii, J. R., 1966, *ApJ*, 146, 480
- Jokipii, J. R., & Parker, E. N., 1969, *ApJ*, 155, 777
- Jokipii, J. R., 1973, *ARA&A*, 11, 1
- Jokipii, J. R., Kota, J. & Giacalone, J., 1993, *GRL*, 20, 17, 1759
- Kaiser T. B. Birmingham, T. J., & Jones, F. C., 1978, *Phys. Fluids.*, 21, 361

- I. Katz, J. Anderson, J. Polk and J. Brophy, 2003, *J. of Propulsion and Power*,
19, 4, 595
- Kolmogorov, A., 1941, *Dokl. Akad. Nauk SSSR*, 31, 538
- Fermi, E., On the origin of cosmic radiation, 1949, *Phys. Rev.*, 75, 1169
- Laitinen, T. 2013, *ApJ*, 764, 168
- Luhmann, J. G. 1976, *J. Geophys. Res.*, 81, 2089
- Matthaeus, W.H., Goldstein, M.L., 1982, *J. Geophys. Res.* 87(A8), 6011
- Matthaeus, W. H., Goldstein, M. L., & Roberts, D. A., 1990, *J. Geophys. Res.*
95, 20673
- Matthaeus, W. H., Qin, G., Bieber, J. W., & Zank, G. P., 2003, *ApJ*, 590L, 53
- Matthaeus, W.H., Dasso, S., Weygand, J.M., Milano, L.J., Smith, C.W.,
Kivelson, M.G., 2005, *Phys. Rev. Lett.* 95, 231101
- Matthaeus, W. H., Servidio, S., Dmitruk, P., Carbone, V., Oughton, S., Wan,
M., and Osman, K. T., 2012, *ApJ*, 750, 103
- McComas, D. J., et al. 2009, *Science*, 326, 959
- Parker, E. N., 1965, *PSS*, 13, 9
- Podesta J. J., Roberts D. A., and Goldstein M. L., 2007, *ApJ*, 664, 543
- Press, W. H., Flannery, B. P., Teukolsky, S. A., & Vetterling, W. T. 1986,
Numerical Recipes, Cambridge:Cambridge Univ. Press

- Roberts D. A., 2012, PRL, 109, 231102
- Schlickeiser, R., & Achatz, U. 1993, JPP, 49, 63
- Schwadron, N. A., et al. 2009, Science, 326, 966
- Shalchi, A., Büsching, I., Lazarian, A., & Schlickeiser, R. 2010, *ApJ*, 725, 2117
- Shalchi, A., & Hussein, M. 2015, *Astrophysics and Space Science*, 355, 243
- Shebalin, J. V., Matthaeus, W. H., & Montgomery, D., 1983, *J. Plasma Phys.*, 29, 525
- Sun, P. and Jokipii, J. R., 2011, 32nd International Cosmic Rays Conference Proceedings, Vol. 10, 240
- Sun, P. and Jokipii, J. R., 2015, *ApJ*, 815, 65
- Tu, C. Y., & Marsch, E. 1993, *J. Geophys. Res.*, 98, 1257
- Wicks R. T., Chapman S.C., & Dendy R.O., 2009, *Astrophys. J.* 690, 734
- Wicks R. T., Owens, M. J., & Horbury T. S., 2010, *Solar Phys*, 262: 191
- Winske, D. & Omid, N. 1991 4th ISSS
- Wu, C. S., & Davidson, R. C. 1972, *JGR*, 77, 5399
- Yan, H., & Lazarian, A., 2002, *Phys. Rev. L*, 34, 1292
- Yan, H., & Lazarian, A., 2004, *ApJ*, 614, 757

Yan H., & Lazarian A., 2008, *ApJ*, 673, 942